A list of 48 Binary Black Hole mergers

Technical Report · July 2021

DOI: 10.13140/RG.2.2.11329.07526

2 authors:

José Laurindo de Góis Nóbrega Sobrinho
Universidade da Madeira
69 PUBLICATIONS **99** CITATIONS
SEE PROFILE

Sara Melissa Azevedo Freitas
Universidade da Madeira
1 PUBLICATION **0** CITATIONS
SEE PROFILE

A list of 48 Binary Black Hole mergers

Freitas S. M. A.[1], Sobrinho J. L. G.

July 2021

Grupo de Astronomia da Universidade da Madeira
Faculdade de Ciências Exatas e da Engenharia
Universidade da Madeira, Campus da Penteada, 9020-105 Funchal
astro@uma.pt
http://www.uma.pt/astro

Abstract

The first direct Gravitational Wave (GW) detection was made by the Advanced Laser Interferometer Gravitational Wave Observatory (LIGO) on September 14, 2015. The emission was originated when two Black Holes (BHs) forming a Binary Black Hole (BBH) system merged given rise to a single BH. Since then dozens of GW events associated with the merge of compact objects were detected. Here we focus on the 48 GW events related to the merge of BBHs. We summarized the key parameters which characterize each one of these 48 BBH systems and explored some relations between them. In particular we estimated that the amount of energy radiated in the form of GWs is $\approx 5\%$ of the total initial mass of the system. We discussed the origin of the 48 BBHs (stellar or primordial) and conclude that at least in 10 of the cases it is highly probable that the origin is primordial, i.e., the BBH is formed by two individual Primordial Black Holes.

Keywords: black hole physics - gravitational waves - early Universe - stars: black holes - black hole mergers

[1]Freitas S. M. A. was supported by the **Estágios de Verão** 2021 programme, promoted by the **Secretaria Regional da Educação**, through the **Direção Regional de Juventude e Desporto** (DRJD) - Região Autónoma da Madeira.

1 Introduction

The first direct Gravitational Wave (GW) detection was made by the Advanced Laser Interferometer Gravitational Wave Observatory (LIGO) on September 14, 2015 (Abbott et al., 2017c). The event, which consisted on the merger of two Black Holes (BHs) with, respectively, $35.6M_{\odot}$ and $30.6M_{\odot}$ is referred to as GW150914 (Abbott et al., 2016c).

Advanced LIGO and Advanced Virgo have demonstrated a new means to observe the Universe through the detection of GWs. In their first two observing runs (O1 and O2), the LIGO Scientific Collaboration and the Virgo Collaboration (LVC) have reported the detection of GWs from 10 Binary Black Hole (BBH) mergers, and a binary neutron star inspiral. The third observing run (O3) started on April 1, 2019, and was suspended on March 27, 2020 (Abbott et al., 2020b). The results of searches for compact binaries in Advanced LIGO and Advanced Virgo data taken between 1 April 2019 15:00 UTC and 1 October 2019 15:00 UTC are referred to as O3a and those obtained later on, up to march 2020, are refereed to as O3b (Abbott et al., 2021). So far, 48 GW events related to the coalescence of BBHs have been observed (cf. Section 3). The masses of the involved individual BHs are within the range 2–95 $M_{\odot}$, suggesting the existence of an important population of BBHs within that mass range (Abbott et al., 2016d).

In Özel & Freire (2016) the maximum mass for neutron stars is set at $2.01M_{\odot}$ although in Cromartie et al. (2020) a mass of $2.14M_{\odot}$ associated with the millisecond pulsar MSP $J0740 + 6620$ has been reported. The events GW190425 and GW190814 have revealed the existence of compact objects of masses between 1.8 $M_{\odot}$ and 2.7 $M_{\odot}$. In the case of GW190425 the possibility that one or both components of the system are BHs cannot be ruled from GW data (Abbott et al., 2020) and, in the case of GW190814 the primary component is a $\approx 23.2M_{\odot}$ BH and the secondary component $\approx 2.59M_{\odot}$ is either the lightest BH or the heaviest neutron star ever discovered in a double compact-object system (Abbott et al., 2020a). It turns out that although this is above the mass of all known binary neutron stars it is also below the expectations for known BH candidates with stellar origin (Clesse & Garcia-Bellido, 2020). In fact, the lowest-mass BH candidate known to date has an attributed mass of $3.3M_{\odot}$ (Thompson et al., 2019).

On the other hand it's not very likely that individual BH components with masses higher than $\sim 60M_{\odot}$ have directly formed after stellar explosions (Clesse & Garcia-Bellido, 2020). Those masses are larger than those of typical binary BHs formed in astrophysical scenarios at the final stage of stellar evolution of main sequence stars (e.g. Blinnikov et al., 2016; Kohri & Terada, 2018; Sasaki et al., 2018; Scelfo et al., 2018; Belotsky et al., 2019) although the existence of such BBHs from astrophysical origin is not completely excluded (Belczynski et al., 2020).

Based on the observed BH candidates known to date it is possible to establish two mass gaps: i) the so-called lower mass gap between $\sim 2M_{\odot}$ and $\sim 5M_{\odot}$ and ii)

the so-called upper pair-instability mass gap between $\sim 50M_{\odot}$ and $\sim\ 150M_{\odot}$ (Abbott et al., 2019b; Clesse & Garcia-Bellido, 2020). The existence of any BHs found within these mass gaps is hard to explain based on stellar evolution arguments (Clesse & Garcia-Bellido, 2020).

Considering that Primordial Black Holes (PBHs) might have formed in the early Universe as a consequence of the collapse of density fluctuations (see Sobrinho et al., 2016; Sobrinho & Augusto, 2020, and references therein) it is plausible to consider that, at least, a fraction of these BBHs could be of primordial origin (e.g. Bird et al., 2016; Clesse & García-Bellido, 2017; Belotsky et al., 2019; Gow et al., 2020). As a matter of fact the first series of GW observations by LIGO/Virgo have brought their share of surprises, like progenitor masses above expectations, suggesting that they may come from low-metallicity environments if of stellar origin, and low effective spins that are hard to explain in standard stellar evolution scenarios (Clesse & Garcia-Bellido, 2020). All this suggests the need of revising and improving stellar or BH evolution scenarios, or of seriously considering the existence of a new population of BHs of primordial origin (Clesse & Garcia-Bellido, 2020).

In this work we compile the main parameters that characterize the 48 BBH systems associated with some of the detected GW events so far and to try establish some relationships between them. We also explored and discuss the hypothesis that some of those BBH systems are rather of primordial origin than the final result of a binary star system. The paper is organized as follows: in Section 2 we review summarily some key aspects concerning BBHs and their coalescence process leading to a GW emission event and in Section 3 we list the main parameters concerning these BBH merger events observed so far. In Section 4 we explore some relations between the different parameters. Finally, in Section 5 we finish with some conclusions and remarks.

2 Binary Black Holes

An isolated BH is described by only three parameters: mass (m), spin (S) and electric charge (ε). Since in the case of astrophysical BHs we get $\varepsilon \approx 0$ (se e.g. d'Inverno, 1993) here we will consider only BHs with mass and spin, i.e., Kerr BHs.

The two BHs forming a BBH are described by their gravitational masses (m_1, m_2) as well as by their individual spins ($\vec{S_1}$, $\vec{S_2}$) in terms of magnitude and orientation (assuming the BHs in isolation) (Abbott et al., 2016b). Here we assume, without any loss of generality, that $m_1 \geq m_2$ and we will refer to the BH with mass m_1 as the *primary component* and to the BH with mass m_2 as the *secondary component*. The initial total mass of the BBH is given by (Abbott et al., 2016b):

$$M = m_1 + m_2 \tag{1}$$

Other useful quantities relating the BH masses are the so-called reduced mass:

$$\mu = \frac{m_1 m_2}{M} \tag{2}$$

and the (adimensional) mass ratio:

$$q = \frac{m_2}{m_1} \tag{3}$$

Notice that here q is defined such that $0 < q \leq 1$ all the time[2].

The spin corresponds to the angular momentum of the BH about its own rotation axis. The absolute value of the dimensionless spin magnitude for a BH with mass m and spin $\vec{S}$ is given by (Abbott et al., 2017b):

$$a = \left| \frac{cS}{Gm^2} \right| \tag{4}$$

such that $0 \leq a \leq 1$. When $a = 0$ we get a non-rotating BH (i.e., we get a Scharzschild BH) and when $a = 1$ we get an extreme rotating Kerr BH (see e.g. d'Inverno, 1993; Sobrinho, 2003).

On the other hand the angular momentum $\vec{L}$ of the BBH orbit is called the orbital angular momentum (Abbott et al., 2017b). If the BHs spin angular momenta $\vec{S_1}$ and $\vec{S_2}$ are aligned (anti-)parallel to the orbital angular momentum $\vec{L}$, then the orbital motion occurs in a fixed two-dimensional plane, deffined by $\vec{L}$ (Schmidt et al., 2015).

We may consider to a certain extent the Newtonian angular momentum, such that it is normal to the orbital plane of the BBH system. However the total orbital angular momentum differs from this because of Post-Newtonian (PN) corrections (Abbott et al., 2017b). This simple picture changes when the individual spins have some arbitrary orientation. In such generic configurations, the orientations of the individual spins and the orbital plane evolve. In most configurations the binary follows simple precession, where both the spin and orbital angular momenta precess around the binary's total angular momentum (Schmidt et al., 2015; Abbott et al., 2016b):

$$\vec{J} = \vec{L} + \vec{S_1} + \vec{S_2} \tag{5}$$

The direction of the total angular momentum $\vec{J}$ is approximately fixed and is therefore a natural generalization of the orbital angular momentum as characteristic direction in the binary system (Schmidt et al., 2015).

If $\hat{N}$ is the line-of-sight direction of a distant inertial observer (detector), then we can define $\theta = \angle(\hat{N}, \hat{J})$ as the inclination of the BBH (Schmidt et al., 2015). For a binary viewed face-on we get $\cos\theta = \pm 1$ and for a binary observed edge-on we get $\cos\theta = 0$.

[2]Some authors consider instead $q = \frac{m_1}{m_2}$ in which case they get $q \geq 1$ always.

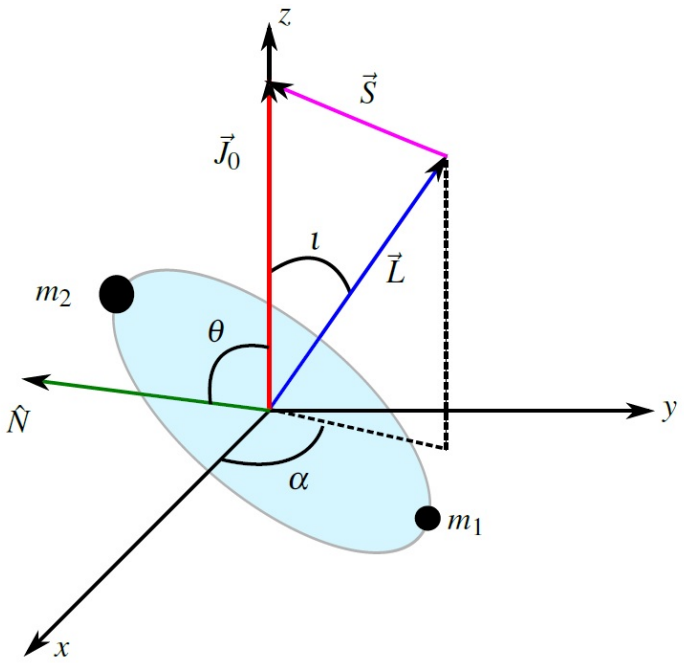

Figure 1: The $\vec{J}_0$ aligned source frame of a precessing BBH with masses m_1 and m_2. Here $\vec{L}$ is the orbital angular momentum of the system whereas $\vec{S} = \vec{S_1} + \vec{S_2}$ is the total spin (cf. equation 5). The angles ι and α are, respectively, the precession angle and the azimuthal angle (cf. equations 6 and 7). On the other hand the angle θ represents the inclination of the BBH with respect to an observer (detector) along the direction $\hat{N}$ (Schmidt et al., 2015).

Here we adopt a Cartesian coordinate system attached to the binary such that at the initial time $\hat{J}_0 \equiv \hat{z}$, which we refer to as the J_0-aligned source frame. Therein, we define the instantaneous direction of the orbital angular momentum, $\hat{L}(t)$ by the two polar angles ($\iota(t)$,$\alpha(t)$). These functions encode the time evolution of the orientation of the orbital plane in the source frame. The precession cone opening angle $\iota(t)$ is defined by (Schmidt et al., 2015):

$$\iota(t) = \arccos(\hat{L}.\hat{J}) \tag{6}$$

and the azimuthal angle $\alpha(t)$ is given by (Schmidt et al., 2015):

$$\alpha(t) = \arctan\left(\frac{L_y}{L_x}\right) \tag{7}$$

The geometry of a precessing configuration is depicted in Figure 1. The azimuth angle is directly related to the precession frequency, i.e., the rate at which $\hat{L}$ precesses $\hat{J}$ (Schmidt et al., 2015):

$$\omega_p(t) = \frac{d\alpha(t)}{dt} \tag{8}$$

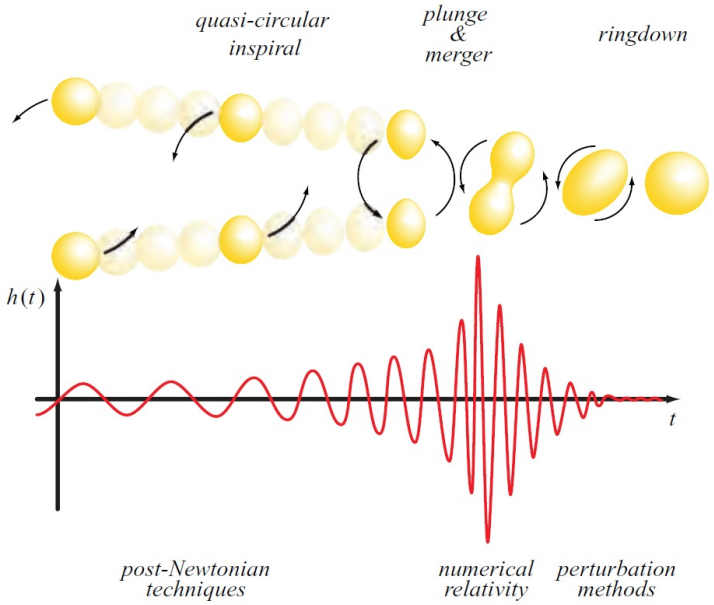

Figure 2: The different stages of compact binary inspiral and coalescence for a BBH. The GW amplitude $h(t)$ is sketched schematically and the analysis technique used for each phase is identified (Baumgarte & Shapiro, 2010). See text (Sections 2.1, 2.2 and 2.3) for more details.

The evolution of BBHs (and other compact binaries such as neutron star binaries, or BH-neutron star binaries) proceeds in several distinct stages. In each stage the orbit progressively decays due to the loss of energy and angular momentum carried away by GWs (see e.g. Kenyon, 1990). Notice that this is in contrast with Newtonian gravity where bodies can follow closed, elliptical orbits (see e.g. Landau & Lifshitz, 1969). Eventually the two BHs spiral into one another and form a single BH: this is called the coalescence of the BBH (Baumgarte & Shapiro, 2010).

This coalescence process can split into three different stages (see Figure 2):

1. inspiral
2. plunge and merger
3. ringdown

Solving the BBH coalescence problem in General Relativity (GR) is quite challenging. Analytic PN expansions are used to determine the early inspiral stage. The late inspiral stage as well as the plunge and merger stage, where the GW amplitude is largest, requires Numerical Relativity (NR) simulations. As for the final ringdown stage it must be treated using BH perturbation methods.

In Figure 3 it is shown, as an example, the signals detected in the case of the GW150914 in 2015. It is remarkable how the wave signal fits the theoretical

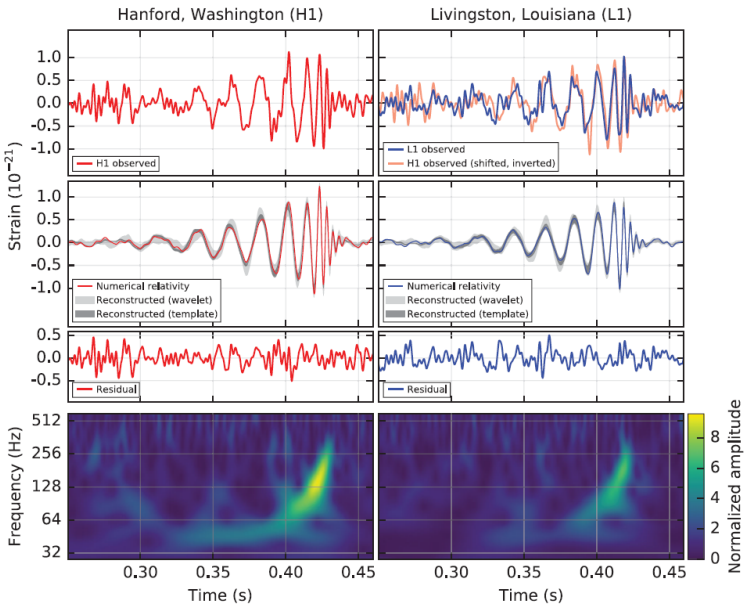

Figure 3: The gravitational-wave event GW150914 observed by the LIGO Hanford (H1, left column panels) and Livingston (L1, right column panels) detectors. Times are shown relative to September 14, 2015 at 09:50:45 UTC. For details see Abbott et al. (2016c).

predictions such as the one represented in Figure 2 which was published five years before the first GW detection.

2.1 The Inspiral stage

The first stage during coalescence is the inspiral which consists of a gradually shrinking orbit that is close to adiabatic (i.e. the process is approximately in an equilibrium state at every step). Mainly PN methods (i.e. Newtonian physics with some modifications to account for relativistic effects) are used to treat this stage which relies on small velocities and weak gravitational fields (Buonanno et al., 2008). In particular the initial part of the inspiral stage turns out to be the longest epoch during the BBH coalescence process.

In GR, gravitational radiation is fully described by two independent, and time-dependent polarizations, h_+ and $h_\times$. Each instrument k measures the strain (Abbott et al., 2016b):

$$h_k = F_k^+ h_+ + F_k^\times h_\times \tag{9}$$

a linear combination of the polarizations weighted by the antenna beam patterns F_k^+ and $F_k^\times$ which depend on the source location in the sky and the polarization of the waves.

During the inspiral and at the leading order, the GW polarizations can be expressed as (Abbott et al., 2016b):

$$h_+(t) = A_{GW}(t)(1 + \cos^2(\theta)) \cos \phi_{GW}(t) \tag{10}$$

$$h_\times(t) = -2A_{GW}(t) \cos(\theta) \sin \phi_{GW}(t) \tag{11}$$

where $A_{GW}(t)$ and $\phi_{GW}(t)$ are, respectively, the GW amplitude and the GW phase.

During the inspiral, the phase evolution ϕ_{GW} can be computed using PN theory. At the leading order, the phase evolution can be approximated by (Abbott et al., 2016b):

$$M_{chirp} \simeq \frac{c^3}{G} \left[\frac{5}{96} \pi^{-8/3} f^{-11/3} \frac{df}{dt} \right]^{3/5} \tag{12}$$

where f is the GW frequency as a function of time t and the mass M_{chirp} is related to the component masses according to (Abbott et al., 2017c):

$$M_{chirp} = \frac{(m_1 m_2)^{3/5}}{M^{1/5}} \tag{13}$$

Equation (12) can be integrated in order to obtain (Abbott et al., 2017c):

$$f^{-8/3}(t) = \frac{(8\pi)^{8/3}}{5} \left(\frac{G M_{chirp}}{c^3} \right)^{5/3} (t_c - t) \tag{14}$$

which does not involve the time derivative of f explicitly, and can therefore be used to calculate M_{chirp}. The constant of integration t_c is the time of coalescence (Abbott et al., 2017c). To leading order, the PN expansion of the GW wave phase depends on the chirp mass making it a very well constrained parameterization of the binary mass (Farr et al., 2016).

Additional parameters enter at each of the following PN orders. The second mass parameter used is the mass ratio q (equation 3). In general from the inspiral, we expect to measure the chirp mass with highest accuracy and only place weak constraints on the mass ratio q and the BH spin components parallel to the orbital angular momentum vector $\vec{L}$ (Abbott et al., 2016b). In general detectors are much less sensitive to the mass ratio, and strong degeneracies with spin make constraints on q even worse (Cutler & Flanagan, 1994). Therefore it is primarily the uncertainty in q that governs the uncertainty in component masses m_1 and m_2 (Farr et al., 2016).

Gravitational-radiation emission causes any existing orbital eccentricity to decay. This means that it is expected that BHs in binary systems should already describe tight circular orbits around each other long before the dominant GW frequencies started to be detected (Baumgarte & Shapiro, 2011). In fact this emission

is efficient in circularizing orbits before the signal enters the sensitive frequency band of the instruments ($\sim 20 - 1000$ Hz). In the observed events so far there are no evidence for any residual eccentricity (Abbott et al., 2016b).

For binary coalescences, the GW frequency evolution is primarily determined by the component masses. For higher mass binaries, merger and ringdown dominate the signal, allowing good measurements of the total mass (equation 1). For lower mass binaries, the inspiral is more important, providing precision measurements of the chirp mass (equation 13). The transition between the two regimes (higher/lower mass binaries) is purely technical depending upon the detectors' sensitivity (Abbott et al., 2017b).

The BH spins play a sub-dominant role in the orbital evolution of the binary, and are more difficult to determine. The spin projections along the direction of the orbital angular momentum affect the inspiral rate of the binary. In particular, spin components aligned (anti-aligned) with $\vec{L}$ increase (decrease) the number of orbits from any given separation to merger with respect to the non-spinning case (Abbott et al., 2016b).

The spin parameter with the largest effect on waveforms, and a correspondingly tight constraint from the data, is a mass-weighted combination of the components of the dimensionless spin vectors of the two BHs that are aligned with the orbital axis, the effective spin (Farr et al., 2017). It is therefore convenient to decompose the spin vectors with respect to $\hat{L}$ into their parallel and orthogonal vector components such that each spin vector (Schmidt et al., 2015):

$$\vec{S_i} = \vec{S_{i\parallel}} + \vec{S_{i\perp}} \tag{15}$$

where $i \in \{1, 2\}$.

The effective inspiral spin parameter (χ_{eff}), a simple mass-weighted linear combination of the spins, is defined by (Abbott et al., 2017b; Farr et al., 2017; Abbott et al., 2016b):

$$\chi_{eff} = \frac{m_1 a_1 \cos(\theta_{LS_1}) + m_2 a_2 \cos(\theta_{LS_2})}{M} \tag{16}$$

where:

$$\theta_{LS_i} = \arccos(\vec{L}.\vec{S_i}) \tag{17}$$

represents the tilt angle between the spin $\vec{S_i}$ and the orbital angular momentum $\vec{L}$ of the system. The value of θ_{LS_i} ranges between 0 (spin aligned with orbital angular momentum) and π (spin anti-aligned). This means that $-1 \leq \chi_{eff} \leq 1$.

PBHs that were produced during a radiation-dominated cosmological epoch have low intrinsic spin magnitude. As a result, a generic prediction of the picture where the LIGO-Virgo BBH events are in part (or all) PBH mergers is that the effective spin parameter is very low (Fernandez & Profumo, 2019) with the possible few exceptions of high-mass events ($M > 50 M_\odot$) (De Luca et al., 2020).

The effective inspiral spin parameter is the most important spin combination for setting the properties of the inspiral phase and remains important through merger. Besides it is approximately constant throughout the orbital evolution (Abbott et al., 2017b).

The in-plane components of the spin control the amount of precession of the orbit. This may be quantified by the effective precession spin parameter χ_p which ranges from 0 (no precession) to 1 (maximal precession) (Abbott et al., 2017b, 2016b).

It is possible to approximate the precession in a generic binary system by combining these four in-plane spin components $S_{1\perp}$ and $S_{2\perp}$ into only one additional spin parameter, a complementary effective precession spin, χ_p (see Schmidt et al., 2015; Gerosa et al., 2021, for detailed discussions).

The in-plane spin components rotate within the orbital plane at different velocities. Because of nutation of the orbital plane, the magnitude of the in-plane spin components oscillates around a mean value, but those oscillations are typically small. To first approximation, one can quantify the level of precession in a binary by averaging over the relative in-plane spin orientation. This is achieved by the following effective precession spin parameter (Abbott et al., 2016b; Schmidt et al., 2015; Gerosa et al., 2021):

$$\chi_p = \frac{c}{B_1 G m_1^2} \max(B_1 S_{1\perp}, B_2 S_{2\perp}) \tag{18}$$

where:

$$B_1 = 2 + \frac{3q}{2} \tag{19}$$

$$B_2 = 2 + \frac{3}{2q} \tag{20}$$

and $S_{1\perp}$ and $S_{2\perp}$ are the components of the spin perpendicular to $\vec{L}$. Here $\chi_p = 0$ corresponds to an aligned-spin (non-precessing) system, and $\chi_p = 1$ to a binary with the maximum level of precession (Abbott et al., 2016b).

2.2 The plunge and merger stage

As the BHs get closer to each other and their velocities increase the BBH undergoes very complicated dynamics. As a consequence the accuracy of the PN expansion degrades, and eventually the full solution of Einstein's equations is needed to accurately describe the evolution of the BBH. This is accomplished using NR (Buonanno et al., 2008; Abbott et al., 2016b).

As the binary shrinks, the frequency and amplitude of the emitted GWs increase (see Figures 2 and 3). The Innermost Stable Circular Orbit (ISCO) is the last complete orbit before the transition to the merger stage in which the two BHs merge into a single BH with the emission of an appreciable amount of energy in the form of GWs (Buonanno et al., 2008).

2.3 The ringdown stage

Immediately following the merger is the ringdown stage in which the now single BH will ring by oscillating in shape as it settles down to stationary equilibrium (Abbott et al., 2016b). Typically an exponentially damped oscillation at constant frequency can be observed as the BH settles to its final state (Figures 2 and 3). To treat this stage, one has to apply perturbation methods to a single BH solution (Baumgarte & Shapiro, 2010, 2011).

The details of the ringdown are primarily governed by the final mass (M_f) and final spin (a_f) of the final BH. In particular, the values of M_f and a_f determine the (constant) frequency and decay time of the BH's ringdown to its final state (Abbott et al., 2020b, 2016b).

The late stage of the coalescence allows us to measure the total mass M which, combined with the measurement of the chirp mass (equation 13) and mass ratio (equation 3) from the early inspiral stage (see Section 2.1), yields estimates of the individual component masses for the binary (Abbott et al., 2016b).

The value of the final spin a_f is a consequence of the conservation of the angular momentum in which the total angular momentum of the system is converted partially into the spin of the remnant BH and partially radiated away in GWs during the merger. Therefore, the final spin is more precisely determined than either of the spins of the individual BHs (Abbott et al., 2016b).

Spins are a fundamental property of BHs. Additionally, their magnitude and orientation with respect to the orbital angular momentum carry an imprint of the evolutionary history of a BBH that could help in identifying the formation channel, such as distinguishing binaries formed in the field from those produced through captures in dense stellar environments (Abbott et al., 2016b).

Systems formed through dynamical interactions among already-compact objects are expected to have isotropic spin orientations, whereas binaries formed from pairs of stars born together are more likely to have spins preferentially aligned with the binary orbital angular momentum (Farr et al., 2017).

The masses (m_1, m_2) and spins (a_1, a_2) of the BHs in a (circular) binary are the only parameters needed to determine the final mass M_f and the final spin a_f of the BH that is produced at the end of the merger. Appropriate relations are embedded intrinsically in the waveform models used in the analysis, but they do not give direct access to the parameters of the remnant BH (see Abbott et al., 2016b, an references therein for a detailed discussion).

It is possible to obtain the angular momentum of the final BH in terms of the initial configuration of the system by a phenomenological approach rather than by evolving the system numerically (Buonanno et al., 2008). This approach is based on the assumptions that: i) to first order, the mass of the system is conserved (less than 10% is converted into energy); ii) the magnitude of the individual spins of the BHs will remain approximately constant, since both spin-spin and spin-orbit couplings are small, and radiation falling into the BHs affects the spins by a small amount; iii) the system radiates much of its angular momentum in the long inspiral

stage until it reaches the ISCO, at which point the dynamics quickly leads to the merger of the two BHs (Buonanno et al., 2008).

During the merger and ringdown phases the total mass and angular momentum of the system change by only a small amount (Buonanno et al., 2008). Thus, to estimate the contribution of the orbital angular momentum to the final angular momentum of the BH, it is sufficient to adopt the orbital angular momentum of a test-particle orbiting at the ISCO of a Kerr BH with a spin parameter equal to a_f (Buonanno et al., 2008).

Bringing all these assumptions together, we may express the spin of the final BH as (Buonanno et al., 2008):

$$\frac{a_f}{M} = \frac{L_{orb}}{M^2} + \frac{m_1 a_1}{M^2} + \frac{m_2 a_2}{M^2} \tag{21}$$

where L_{orb} is the orbital angular momentum of a particle at the ISCO of a Kerr BH with spin parameter a_f. Considering equatorial orbits evaluated at r_{ISCO} we get expressions relating r_{ISCO} and a_f for both prograde and retrograde orbits (for details see Buonanno et al., 2008, and references therein). The use of the prograde or retrograde case depends on whether the final spin is aligned or anti-aligned with the initial orbital angular momentum.

As the GW signal travels from the source to the detector its frequency is redshifted by a factor $(1 + z)$ where z is the cosmological redshift (e.g. Hogg, 1999). For a system involving only BHs, the observed signal is identical to that from a source in the rest frame of the detector with total mass (Cutler & Flanagan, 1994; Abbott et al., 2021):

$$M_{detector} = (1 + z) M_{source} \tag{22}$$

In GR there is no intrinsic mass or length scale. As a consequence a redshifting of frequency is indistinguishable from a rescaling of the masses by the same factor on the dimensionless quantity that incorporates frequency $\frac{fGm}{c^3}$ (Abbott et al., 2016b). We therefore measure redshifted masses, which are related to source frame masses according to equation (22).

The source's luminosity distance D_L (see Hogg, 1999) is inferred from the signal amplitude A_{GW} (cf. equations 10 and 11). The amplitude A_{GW} also scales linearly with the mass and is inversely proportional to the comoving distance in an expanding universe. Therefore, A_{GW} scales inversely with the D_L (Abbott et al., 2016b):

$$A_{GW} \propto \frac{1}{D_L} \tag{23}$$

The source's luminosity distance D_L (Hogg, 1999) is inferred from the signal amplitude A_{GW} which is inversely proportional to the distance, but also depends upon the binary's inclination angle with respect to the observer (θ). Motion occurs in a

fixed two-dimensional plane, defined by $\vec{L}$, which is also the **direction of dominant GW energy emission** (Schmidt et al., 2015). For a binary viewed face-on ($\cos\theta = \pm 1$), GWs are circularly polarized, whereas for a binary observed edge-on ($\cos\theta = 0$), GWs are linearly polarized (Abbott et al., 2016b). This degeneracy is a significant source of uncertainty (Abbott et al., 2017b).

From the GW signal alone we can directly measure the luminosity distance but not the redshift (cf. equation 23). However in order to convert the masses measured in the detector frame to physical source-frame masses, the redshift of the source is required (cf. equation 22). Within the theory of GR redshift and luminosity distance could be related through the expression (Fanizza et al., 2020):

$$D_L(z) = (1+z)\int_0^z \frac{dz'}{H(z')} \tag{24}$$

where the function H represents the Hubble parameter (e.g. Sobrinho, 2011).

The evaluation of the final mass (at the source frame) provides an estimate of the total energy (mass) radiated in the form of GWs. We may write (Abbott et al., 2016b):

$$M_{rad} = M - M_f \tag{25}$$

where all the masses must be considered at the source frame (cf. equation 22).

3 THe BBH merger events observed so far

The list of parameters needed to fully characterize a BBH merger event is quite extensive. We opted to divide those parameters into three different families (mass, spin and distance/energy) allocating a table for each case. (cf. Tables 1, 2 and 3). The majority of the presented values were retrieved from the literature. In some cases we were unable to find out in the literature the value associated with a particular parameter. Whenever possible we determine these values based on the known values of other related parameters. In order to distinguish such situations we marked the corresponding values with a $*$.

In Table 1 we show the values of the parameters directly related to the masses of the individual BHs or to the final BH for all the 48 GW events associated with BBH mergers. Besides the masses m_1 and m_2 we show the total mass M (equation 1), chirp mass M_{chirp} (cf. equations 12, 13 and 14), final mass M_f and mass ratio q (equation 3).

In Table 2 we show the adimensional spin parameter (see equation 4) for the primary (a_1) and secondary BHs (a_2), the effective inspiral spin χ_{eff} (equation 16) and the effective precession spin χ_p (equation 18) for the BBH as well as the spin of the final BH (cf. equation 21). Notice that the set of spin values (a_1,a_2) is rather incomplete. We manage to find the values of a_1 and a_2 for only, respectively, 13 and

10 events (for a total of 48 events). In three cases (GW190425, GW190719_215514, GW190909_114149) the value of χ_p is also absent. Finally in the case of GW190425 the value of a_f also lacks.

Finally, in Table 3 we show the luminosity distance (D_L) and cosmological redshift (z) for each GW event (cf. equations 23 and 24). We also show the value of the luminosity peak (L_{peak}) and the radiated energy (M_{rad}, equation 25) for the first 10 events, i.e., for the BBH mergers detected during the two first observing runs (O1 and O2).

We calculated the radiated energy (M_{rad}) for the missing values of the remaining 38 events using equation (25). Given the uncertainties on the values of M and M_f on these events, the uncertainty of the final result M_{rad} would be, in absolute value, $\gg M_{rad}$. For example, calculating M_{rad} for GW190909_114149, using equation (25) and calculating the error using standard deviation, we get $3.0M_{\odot}\pm78.4M_{\odot}$, which is absurd. Therefore, we opted to determine the relative error associated with each of the M_{rad} values known to date and we verified that these values would vary between 11.1% and 37.5%, such that we used the greatest of these values to estimate the uncertainty associated to each of the missing values of M_{rad}.

Notice that besides the parameters shown on Tables 1, 2 and 3 there are a few additional parameters with which we could get a more complete picture for each event. In fact to fully describe the BBH we would need nine additional parameters: right ascension (α), declination (δ), binary's orbital inclination angle (θ), polarization (ψ), coalescence time (t_c), phase of coalescence (ϕ_c), orbit eccentricity (ϵ) and the periapsis (p) of the system (Abbott et al., 2016b).

4 Exploring the data

In Figure 4 we represent the relation between the masses m_1 and m_2 ($m_1 \geq m_2$) for the 48 BBHs shown on Table 1. We divided into five regions according to the so-called lower and upper mass gaps. The small region labeled I, accommodating the single event GW190425 represents the lower mass gap and the region II, which accommodate only a single event (GW190521) represents the upper mass gap. As it was mentioned before (see Section 1) the existence of any BBHs within these regions (in this case we have two) is hard to explain based on typical stellar evolution arguments. On the other hand the BBHs located on region III, in fact the majority of the BBHs on our list, are those which existence is in accordance with stellar evolution arguments. Besides these three we have tow hybrid regions. In region IV we have seven BBHs (GW170729, GW190519_153544, GW190602_175927, GW190620_030421, GW190701_203306, GW190706_222641, GW190929_012149) for which although m_1 fits the upper mass gap, m_2 does not and, finally, in region V we have the case GW190814 for which m_2 fits the lower mass gap but m_1 does not. In Figures 5 and 6 we can see the distribution of m_1 and m_2, respectively.

In Figure 7 we show the relation between the spin of the primary BH, a_1, and

Table 1: **GW event**: name given to the gravitional wave event; $\boldsymbol{m_1(M_\odot)}$: mass of the primary BH; $\boldsymbol{m_2(M_\odot)}$: mass of the secondary BH; $\boldsymbol{M(M_\odot)}$: joint mass of the two BHs before they merge (the values with * were calculated using equation (1) and the error was calculated using standard deviation); $\boldsymbol{M_{chirp}(M_\odot)}$: chirp mass (cf. equations 12, 13 and 14); $\boldsymbol{M_f(M_\odot)}$: mass of the final BH; $\boldsymbol{q(m_2/m_1)}$: mass ratio (the values with * were calculated using equation (3) and the error was calculated using standard deviation); **References**: [**1**] Abbott et al. (2019a); [**2**] Abbott et al. (2016a); [**4**] Abbott et al. (2021); [**5**] Abbott et al. (2017a); [**7**] Abbott et al. (2017b); [**9**] The LIGO Scientific Collaboration et al. (2020); [**10**] Abbott et al. (2020a).

	GW event	$m_1(M_\odot)$	$m_2(M_\odot)$	$M(M_\odot)$	$M_{chirp}(M_\odot)$	$M_f(M_\odot)$	q	Ref.
1	GW150914	$35.6^{+4.7}_{-3.1}$	$30.6^{+3.0}_{-4.4}$	$65.3^{+4.1}_{-3.4}$	$28.6^{+1.7}_{-1.5}$	$63.1^{+3.4}_{-3.0}$	0.860±0.168*	[1], [2]
2	GW151012	$23.2^{+14.9}_{-5.5}$	$13.6^{+4.1}_{-4.8}$	36.8±4.4*	$15.2^{+2.1}_{-1.2}$	$35.6^{+10.8}_{-3.8}$	0.586±0.430*	[1]
3	GW151226	$13.7^{+8.8}_{-3.2}$	$7.7^{+2.2}_{-2.5}$	$21.8^{+5.9}_{-1.7}$	$8.9^{+0.3}_{-0.3}$	$20.5^{+6.4}_{-1.5}$	0.562±0.405*	[1], [2]
4	GW170104	$30.8^{+7.3}_{-5.6}$	$20.0^{+4.9}_{-4.6}$	$50.7^{+5.9}_{-5.0}$	$21.4^{+2.2}_{-1.8}$	$48.9^{+5.1}_{-4.0}$	0.649±0.221*	[1], [7]
5	GW170608	$11.0^{+5.5}_{-1.7}$	$7.6^{+1.4}_{-2.2}$	18.6±2.8*	$7.9^{+0.2}_{-0.2}$	$17.8^{+3.4}_{-0.7}$	0.691±0.399*	[1]
6	GW170729	$50.2^{+16.2}_{-10.2}$	$34.0^{+9.1}_{-10.1}$	84.2±5.1*	$35.4^{+6.5}_{-4.8}$	$79.5^{+14.7}_{-10.2}$	0.677±0.297*	[1]
7	GW170809	$35.0^{+8.3}_{-5.9}$	$23.8^{+5.1}_{-5.2}$	58.8±3.7*	$24.9^{+2.1}_{-1.7}$	$56.3^{+5.2}_{-3.8}$	0.68±0.22*	[1]
8	GW170814	$30.6^{+5.6}_{-3.0}$	$25.2^{+2.8}_{-4.0}$	$55.9^{+3.4}_{-2.7}$	$24.1^{+1.4}_{-1.1}$	$53.2^{+3.2}_{-2.4}$	0.824±0.200*	[1], [5]
9	GW170818	$35.4^{+7.5}_{-4.7}$	$26.7^{+4.3}_{-5.2}$	62.1±3.6*	$26.5^{+2.1}_{-1.7}$	$59.4^{+4.9}_{-3.8}$	0.754±0.217*	[1]
10	GW170823	$39.5^{+11.2}_{-6.7}$	$29.0^{+6.7}_{-7.8}$	68.5±4.4*	$29.2^{+4.6}_{-3.6}$	$65.4^{+10.1}_{-7.4}$	0.734±0.287*	[1]
11	GW190408_181802	$24.6^{+5.1}_{-3.4}$	$18.4^{+3.3}_{-3.6}$	$43.0^{+4.2}_{-3.0}$	$18.3^{+1.9}_{-1.2}$	$41.1^{+3.9}_{-2.8}$	0.748±0.213*	[4]
12	GW190412	$30.1^{+4.7}_{-5.1}$	$8.3^{+1.6}_{-0.9}$	$38.4^{+3.8}_{-3.7}$	$13.3^{+0.4}_{-0.3}$	$37.3^{+3.9}_{-3.8}$	$0.28^{+0.12}_{-0.07}$	[4], [9]
13	GW190413_052954	$34.7^{+12.6}_{-8.1}$	$23.7^{+7.3}_{-6.7}$	$58.6^{+13.3}_{-9.7}$	$24.6^{+5.5}_{-4.1}$	$56.0^{+12.5}_{-9.2}$	0.683±0.325*	[4]
14	GW190413_134308	$47.5^{+13.5}_{-10.7}$	$31.8^{+11.7}_{-10.8}$	$78.8^{+17.4}_{-11.9}$	$33.0^{+8.2}_{-5.4}$	$75.5^{+16.4}_{-11.4}$	0.669±0.311*	[4]

(continues on next page)

Table 1 (continued).

	GW event	$m_1(M_\odot)$	$m_2(M_\odot)$	$M(M_\odot)$	$M_{chirp}(M_\odot)$	$M_f(M_\odot)$	q	Ref.
15	GW190421_213856	$41.3^{+10.4}_{-6.9}$	$31.9^{+8.0}_{-8.8}$	$72.9^{+13.4}_{-9.2}$	$31.2^{+5.9}_{-4.2}$	$69.7^{+12.5}_{-8.7}$	0.772±0.288*	[4]
16	GW190424_180648	$40.5^{+11.1}_{-7.3}$	$31.8^{+7.6}_{-7.7}$	$72.6^{+13.3}_{-10.7}$	$31.0^{+5.8}_{-4.6}$	$68.9^{+12.4}_{-10.1}$	0.785±0.287*	[4]
17	GW190425	$2.0^{+0.6}_{-0.3}$	$1.4^{+0.3}_{-0.3}$	$3.4^{+0.3}_{-0.1}$	$1.44^{+0.02}_{-0.02}$		0.7±0.3*	[4]
18	GW190503_185404	$43.3^{+9.2}_{-8.1}$	$28.4^{+7.7}_{-8.0}$	$71.7^{+9.4}_{-8.3}$	$30.2^{+4.4}_{-4.2}$	$68.6^{+8.8}_{-7.7}$	0.656±0.231*	[4]
19	GW190512_180714	$23.3^{+5.3}_{-5.8}$	$12.6^{+3.6}_{-2.5}$	$35.9^{+3.8}_{-3.5}$	$14.6^{+1.3}_{-1.0}$	$34.5^{+3.8}_{-3.5}$	0.541±0.205*	[4]
20	GW190513_205428	$35.7^{+9.5}_{-9.2}$	$18.0^{+7.7}_{-4.1}$	$53.9^{+8.6}_{-5.9}$	$21.6^{+3.8}_{-1.9}$	$51.6^{+8.2}_{-5.8}$	0.504±0.254*	[4]
21	GW190514_065416	$39.0^{+14.7}_{-8.2}$	$28.4^{+9.3}_{-8.8}$	$67.2^{+18.7}_{-10.8}$	$28.5^{+7.9}_{-4.8}$	$64.5^{+17.9}_{-10.4}$	0.728±0.364*	[4]
22	GW190517_055101	$37.4^{+11.7}_{-7.6}$	$25.3^{+7.0}_{-7.3}$	$63.5^{+9.6}_{-9.6}$	$26.6^{+4.0}_{-4.0}$	$59.3^{+9.1}_{-8.9}$	0.676±0.288*	[4]
23	GW190519_153544	$66.0^{+10.7}_{-12.0}$	$40.5^{+11.0}_{-11.1}$	$106.6^{+13.5}_{-14.8}$	$44.5^{+6.4}_{-7.1}$	$101.0^{+12.4}_{-13.8}$	0.614±0.202*	[4]
24	GW190521	$95.3^{+28.7}_{-18.9}$	$69.0^{+22.7}_{-23.1}$	$163.9^{+39.2}_{-23.5}$	$69.2^{+17.0}_{-10.6}$	$156.3^{+36.8}_{-22.4}$	0.724±0.326*	[4], [8]
25	GW190521_074359	$42.2^{+5.9}_{-4.8}$	$32.8^{+5.4}_{-6.4}$	$74.7^{+7.0}_{-4.8}$	$32.1^{+3.2}_{-2.5}$	$71.0^{+6.5}_{-4.4}$	0.777±0.187*	[4]
26	GW190527_092055	$36.5^{+16.4}_{-9.0}$	$22.6^{+10.5}_{-8.1}$	$59.1^{+21.3}_{-9.8}$	$24.3^{+9.1}_{-4.2}$	$56.4^{+20.2}_{-9.3}$	0.619±0.400*	[4]
27	GW190602_175927	$69.1^{+15.7}_{-13.0}$	$47.8^{+14.3}_{-17.4}$	$116.3^{+19.0}_{-15.6}$	$49.1^{+9.1}_{-8.5}$	$110.9^{+17.7}_{-14.9}$	0.692±0.297*	[4]
28	GW190620_030421	$57.1^{+16.0}_{-12.7}$	$35.5^{+12.2}_{-12.3}$	$92.1^{+18.5}_{-13.1}$	$38.3^{+8.3}_{-6.5}$	$87.2^{+16.8}_{-12.1}$	0.622±0.277*	[4]
29	GW190630_185205	$35.1^{+6.9}_{-5.6}$	$23.7^{+5.2}_{-5.1}$	$59.1^{+4.6}_{-4.8}$	$24.9^{+2.1}_{-2.1}$	$56.4^{+4.4}_{-4.6}$	0.675±0.199*	[4]
30	GW190701_203306	$53.9^{+11.8}_{-8.0}$	$40.8^{+8.7}_{-12.0}$	$94.3^{+12.1}_{-9.5}$	$40.3^{+5.4}_{-4.9}$	$90.2^{+11.3}_{-8.9}$	0.757±0.278*	[4]
31	GW190706_222641	$67.0^{+14.6}_{-16.2}$	$38.2^{+14.6}_{-13.3}$	$104.1^{+20.2}_{-13.9}$	$42.7^{+10.0}_{-7.0}$	$99.0^{+18.3}_{-13.5}$	0.570±0.258*	[4]

(continues on next page)

Table 1 (continued).

	GW event	$m_1(M_\odot)$	$m_2(M_\odot)$	$M(M_\odot)$	$M_{chirp}(M_\odot)$	$M_f(M_\odot)$	q	Ref.
32	GW190707_093326	$11.6^{+3.3}_{-1.7}$	$8.4^{+1.4}_{-1.7}$	$20.1^{+1.9}_{-1.3}$	$8.5^{+0.6}_{-0.5}$	$19.2^{+1.9}_{-1.3}$	0.724±0.253*	[4]
33	GW190708_232457	$17.6^{+4.7}_{-2.3}$	$13.2^{+2.0}_{-2.7}$	$30.9^{+2.5}_{-1.8}$	$13.2^{+0.9}_{-0.6}$	$29.5^{+2.5}_{-1.8}$	0.750±0.252*	[4]
34	GW190719_215514	$36.5^{+18.0}_{-10.3}$	$20.8^{+9.0}_{-7.2}$	$57.8^{+18.3}_{-10.7}$	$23.5^{+6.5}_{-4.0}$	$54.9^{+17.3}_{-10.2}$	0.570±0.374*	[4]
35	GW190720_000836	$13.4^{+6.7}_{-3.0}$	$7.8^{+2.3}_{-2.2}$	$21.5^{+4.3}_{-2.3}$	$8.9^{+0.5}_{-0.8}$	$20.4^{+4.5}_{-2.2}$	0.582±0.338*	[4]
36	GW190727_060333	$38.0^{+9.5}_{-6.2}$	$29.4^{+7.1}_{-8.4}$	$67.1^{+11.7}_{-8.0}$	$28.6^{+5.3}_{-3.7}$	$63.8^{+10.9}_{-7.5}$	0.774±0.294*	[4]
37	GW190728_064510	$12.3^{+7.2}_{-2.2}$	$8.1^{+1.7}_{-2.6}$	$20.6^{+4.5}_{-1.3}$	$8.6^{+0.5}_{-0.3}$	$19.6^{+4.7}_{-1.3}$	0.659±0.440*	[4]
38	GW190731_140936	$41.5^{+12.2}_{-9.0}$	$28.8^{+9.7}_{-9.5}$	$70.1^{+15.8}_{-11.3}$	$29.5^{+7.1}_{-5.2}$	$67.0^{+14.6}_{-10.8}$	0.694±0.310*	[4]
39	GW190803_022701	$37.3^{+10.6}_{-7.0}$	$27.3^{+7.8}_{-8.2}$	$64.5^{+12.6}_{-9.0}$	$27.3^{+5.7}_{-4.1}$	$61.7^{+11.8}_{-8.5}$	0.732±0.303*	[4]
40	GW190814	$23.2^{+1.1}_{-1.0}$	$2.59^{+0.08}_{-0.09}$	$25.8^{+1.0}_{-0.9}$	$6.09^{+0.06}_{-0.06}$	$25.6^{+1.1}_{-0.9}$	$0.112^{+0.008}_{-0.009}$	[10]
41	GW190828_063405	$32.1^{+5.8}_{-4.0}$	$26.2^{+4.6}_{-4.8}$	$58.0^{+7.7}_{-4.8}$	$25.0^{+3.4}_{-2.1}$	$54.9^{+7.2}_{-4.3}$	0.816±0.210*	[4]
42	GW190828_065509	$24.1^{+7.0}_{-7.2}$	$10.2^{+3.6}_{-2.1}$	$34.4^{+5.4}_{-4.4}$	$13.3^{+1.2}_{-1.0}$	$33.1^{+5.5}_{-4.5}$	0.423±0.196*	[4]
43	GW190909_114149	$45.8^{+52.7}_{-13.3}$	$28.3^{+13.4}_{-12.7}$	$75.0^{+55.9}_{-17.6}$	$30.9^{+17.2}_{-7.5}$	$72.0^{+54.9}_{-16.8}$	0.618±0.769*	[4]
44	GW190910_112807	$43.9^{+7.6}_{-6.1}$	$35.6^{+6.3}_{-7.2}$	$79.6^{+9.3}_{-9.1}$	$34.3^{+4.1}_{-4.1}$	$75.8^{+8.5}_{-8.6}$	0.811±0.216*	[4]
45	GW190915_235702	$35.3^{+9.5}_{-6.4}$	$24.4^{+5.6}_{-6.1}$	$59.9^{+7.5}_{-6.4}$	$25.3^{+3.2}_{-2.7}$	$57.2^{+7.1}_{-6.0}$	0.691±0.254*	[4]
46	GW190924_021846	$8.9^{+7.0}_{-2.0}$	$5.0^{+1.4}_{-1.9}$	$13.9^{+5.1}_{-1.0}$	$5.8^{+0.2}_{-0.2}$	$13.3^{+5.2}_{-1.0}$	0.562±0.491*	[4]
47	GW190929_012149	$80.8^{+33.0}_{-33.2}$	$24.1^{+19.3}_{-10.6}$	$104.3^{+34.9}_{-25.2}$	$35.8^{+14.9}_{-8.2}$	$101.5^{+33.6}_{-25.3}$	0.298±0.268*	[4]
48	GW190930_133541	$12.3^{+12.4}_{-2.3}$	$7.8^{+1.7}_{-3.3}$	$20.3^{+8.9}_{-1.5}$	$8.5^{+0.5}_{-0.5}$	$19.4^{+9.2}_{-1.5}$	0.634±0.693*	[4]

Table 2: **GW event**: name given to the gravitional wave event; $\boldsymbol{a_1}$: spin of the primary BH (equation 4); $\boldsymbol{a_2}$: spin of the secondary BH (equation 4); $\boldsymbol{\chi_{eff}}$: effective inspiral spin (equation 16); $\boldsymbol{\chi_p}$: effective precession spin (equation 18); $\boldsymbol{a_f}$: spin of the final BH (equation 21); **References**: [**1**] Abbott et al. (2019a); [**2**] Abbott et al. (2016a); [**3**] De et al. (2019); [**4**] Abbott et al. (2021); [**6**] Gerosa et al. (2021); [**7**] Abbott et al. (2017b); [**8**] Abbott et al. (2020b); [**9**] The LIGO Scientific Collaboration et al. (2020); [**10**] Abbott et al. (2020a).

	GW event	a_1	a_2	χ_{eff}	χ_p	a_f	Ref.
1	GW150914	$0.32^{+0.47}_{-0.29}$	$0.48^{+0.47}_{-0.43}$	$-0.01^{+0.12}_{-0.13}$	$0.32^{+0.41}_{-0.26}$	$0.69^{+3.4}_{-3.0}$	[1], [2], [6]
2	GW151012			$0.05^{+0.31}_{-0.20}$	$0.31^{+0.40}_{-0.24}$	$0.67^{+0.13}_{-0.11}$	[1], [6]
3	GW151226	$0.49^{+0.37}_{-0.42}$	$0.52^{+0.43}_{-0.47}$	$0.18^{+0.20}_{-0.12}$	$0.42^{+0.29}_{-0.27}$	$0.74^{+0.07}_{-0.05}$	[1], [2], [6]
4	GW170104	$0.45^{+0.46}_{-0.40}$	$0.47^{+0.46}_{-0.43}$	$-0.04^{+0.17}_{-0.21}$	$0.37^{+0.36}_{-0.28}$	$0.66^{+0.08}_{-0.11}$	[1], [6], [7]
5	GW170608	$0.32^{+0.47}_{-0.29}$	$0.43^{+0.49}_{-0.39}$	$0.03^{+0.19}_{-0.07}$	$0.31^{+0.35}_{-0.24}$	$0.69^{+0.04}_{-0.04}$	[1], [3], [6]
6	GW170729	$0.60^{+0.34}_{-0.51}$	$0.57^{+0.38}_{-0.50}$	$0.37^{+0.21}_{-0.25}$	$0.42^{+0.36}_{-0.28}$	$0.81^{+0.07}_{-0.13}$	[1], [3], [6]
7	GW170809	$0.34^{+0.53}_{-0.31}$	$0.40^{+0.51}_{-0.37}$	$0.08^{+0.17}_{-0.17}$	$0.34^{+0.38}_{-0.26}$	$0.70^{+0.08}_{-0.09}$	[1], [3], [6]
8	GW170814	$0.53^{+0.42}_{-0.48}$	$0.46^{+0.47}_{-0.42}$	$0.07^{+0.12}_{-0.12}$	$0.49^{+0.32}_{-0.37}$	$0.72^{+0.07}_{-0.05}$	[1], [3], [6]
9	GW170818	$0.56^{+0.38}_{-0.50}$	$0.50^{+0.44}_{-0.45}$	$-0.09^{+0.18}_{-0.21}$	$0.51^{+0.29}_{-0.35}$	$0.67^{+0.07}_{-0.08}$	[1], [3], [6]
10	GW170823	$0.44^{+0.48}_{-0.40}$	$0.45^{+0.48}_{-0.41}$	$0.09^{+0.22}_{-0.26}$	$0.45^{+0.41}_{-0.35}$	$0.72^{+0.09}_{-0.12}$	[1], [3], [6]
11	GW190408_181802			$-0.03^{+0.14}_{-0.19}$	$0.39^{+0.37}_{-0.31}$	$0.67^{+0.06}_{-0.07}$	[4], [6]
12	GW190412	$0.44^{+0.16}_{-0.22}$		$0.25^{+0.08}_{-0.11}$	$0.31^{+0.19}_{-0.16}$	$0.67^{+0.05}_{-0.06}$	[4], [6], [9]
13	GW190413_052954			$-0.01^{+0.29}_{-0.34}$	$0.42^{+0.42}_{-0.32}$	$0.68^{+0.12}_{-0.13}$	[4], [6]
14	GW190413_134308			$-0.03^{+0.25}_{-0.29}$	$0.56^{+0.36}_{-0.42}$	$0.68^{+0.10}_{-0.12}$	[4], [6]
15	GW190421_213856			$-0.06^{+0.22}_{-0.27}$	$0.49^{+0.40}_{-0.37}$	$0.67^{+0.10}_{-0.11}$	[4], [6]

(continues on next page)

Table 2 (continued).

	GW event	a_1	a_2	χ_{eff}	χ_p	a_f	Ref.
16	GW190424_180648			$0.13^{+0.22}_{-0.22}$	$0.52^{+0.37}_{-0.37}$	$0.74^{+0.09}_{-0.09}$	[4], [6]
17	GW190425			$0.06^{+0.11}_{-0.05}$			[4]
18	GW190503_185404			$-0.03^{+0.20}_{-0.26}$	$0.39^{+0.41}_{-0.29}$	$0.66^{+0.09}_{-0.12}$	[4], [6]
19	GW190512_180714			$0.03^{+0.12}_{-0.13}$	$0.23^{+0.37}_{-0.18}$	$0.65^{+0.07}_{-0.07}$	[4], [6]
20	GW190513_205428			$0.11^{+0.28}_{-0.17}$	$0.30^{+0.40}_{-0.22}$	$0.68^{+0.14}_{-0.12}$	[4], [6]
21	GW190514_065416			$-0.19^{+0.29}_{-0.32}$	$0.47^{+0.39}_{-0.34}$	$0.63^{+0.11}_{-0.15}$	[4], [6]
22	GW190517_055101			$0.52^{+0.19}_{-0.19}$	$0.48^{+0.31}_{-0.28}$	$0.87^{+0.05}_{-0.07}$	[4], [6]
23	GW190519_153544			$0.31^{+0.20}_{-0.22}$	$0.45^{+0.34}_{-0.29}$	$0.79^{+0.07}_{-0.13}$	[4], [6]
24	GW190521	$0.69^{+0.27}_{-0.62}$	$0.73^{+0.24}_{-0.64}$	$0.03^{+0.32}_{-0.39}$	$0.67^{+0.26}_{-0.44}$	$0.71^{+0.12}_{-0.16}$	[4], [6], [8]
25	GW190521_074359			$0.09^{+0.10}_{-0.13}$	$0.40^{+0.32}_{-0.29}$	$0.72^{+0.05}_{-0.07}$	[4], [6]
26	GW190527_092055			$0.11^{+0.28}_{-0.28}$	$0.46^{+0.42}_{-0.35}$	$0.71^{+0.12}_{-0.16}$	[4], [6]
27	GW190602_175927			$0.07^{+0.25}_{-0.24}$	$0.43^{+0.41}_{-0.32}$	$0.70^{+0.10}_{-0.14}$	[4], [6]
28	GW190620_030421			$0.33^{+0.22}_{-0.25}$	$0.43^{+0.37}_{-0.29}$	$0.79^{+0.08}_{-0.15}$	[4], [6]
29	GW190630_185205			$0.10^{+0.12}_{-0.13}$	$0.31^{+0.32}_{-0.23}$	$0.70^{+0.05}_{-0.07}$	[4], [6]
30	GW190701_203306			$-0.07^{+0.23}_{-0.29}$	$0.42^{+0.42}_{-0.31}$	$0.66^{+0.09}_{-0.13}$	[4], [6]
31	GW190706_222641			$0.28^{+0.26}_{-0.29}$	$0.41^{+0.38}_{-0.28}$	$0.78^{+0.09}_{-0.18}$	[4], [6]
32	GW190707_093326			$-0.05^{+0.10}_{-0.08}$	$0.29^{+0.39}_{-0.23}$	$0.66^{+0.03}_{-0.04}$	[4], [6]

(continues on next page)

Table 2 (continued).

	GW event	a_1	a_2	χ_{eff}	χ_p	a_f	Ref.
33	GW190708_232457			$0.02^{+0.10}_{-0.08}$	$0.29^{+0.43}_{-0.24}$	$0.69^{+0.04}_{-0.04}$	[4], [6]
34	GW190719_215514			$0.32^{+0.29}_{-0.31}$		$0.78^{+0.11}_{-0.17}$	[4]
35	GW190720_000836	$0.40^{+0.40}_{-0.35}$		$0.18^{+0.14}_{-0.12}$	$0.33^{+0.43}_{-0.22}$	$0.72^{+0.06}_{-0.05}$	[4], [6]
36	GW190727_060333			$0.11^{+0.26}_{-0.25}$	$0.48^{+0.39}_{-0.36}$	$0.73^{+0.10}_{-0.10}$	[4], [6]
37	GW190728_064510	$0.32^{+0.37}_{-0.28}$		$0.12^{+0.20}_{-0.07}$	$0.29^{+0.37}_{-0.20}$	$0.71^{+0.04}_{-0.04}$	[4], [6]
38	GW190731_140936			$0.06^{+0.24}_{-0.24}$	$0.42^{+0.43}_{-0.32}$	$0.70^{+0.10}_{-0.13}$	[4], [6]
39	GW190803_022701			$-0.03^{+0.24}_{-0.27}$	$0.45^{+0.42}_{-0.34}$	$0.68^{+0.10}_{-0.11}$	[4], [6]
40	GW190814			$-0.002^{+0.060}_{-0.061}$	$0.04^{+0.04}_{-0.03}$	$0.28^{+0.02}_{-0.02}$	[10]
41	GW190828_063405			$0.19^{+0.15}_{-0.16}$	$0.43^{+0.36}_{-0.30}$	$0.75^{+0.06}_{-0.07}$	[4], [6]
42	GW190828_065509			$0.08^{+0.16}_{-0.16}$	$0.29^{+0.40}_{-0.22}$	$0.65^{+0.08}_{-0.08}$	[4], [6]
43	GW190909_114149			$-0.06^{+0.37}_{-0.36}$		$0.66^{+0.15}_{-0.20}$	[4]
44	GW190910_112807			$0.02^{+0.18}_{-0.18}$	$0.41^{+0.39}_{-0.32}$	$0.70^{+0.08}_{-0.07}$	[4], [6]
45	GW190915_235702			$0.02^{+0.20}_{-0.25}$	$0.56^{+0.36}_{-0.39}$	$0.70^{+0.09}_{-0.11}$	[4], [6]
46	GW190924_021846			$0.03^{+0.30}_{-0.09}$	$0.24^{+0.40}_{-0.18}$	$0.67^{+0.05}_{-0.05}$	[4], [6]
47	GW190929_012149			$0.01^{+0.34}_{-0.33}$	$0.39^{+0.43}_{-0.30}$	$0.66^{+0.20}_{-0.31}$	[4], [6]
48	GW190930_133541			$0.14^{+0.31}_{-0.15}$	$0.34^{+0.40}_{-0.24}$	$0.72^{+0.07}_{-0.06}$	[4], [6]

Table 3: **GW event**: name given to the gravitional wave event; $\boldsymbol{D_L(Mpc)}$: luminosity distance (cf. equations 23 and 24); $\boldsymbol{L_{peak}}$: peak luminosity measured in erg s^{-1}; $\boldsymbol{z}$: cosmological redshift; $\boldsymbol{M_{rad}(M_\odot)}$: radiated energy (the values with * were calculated using equation 25); **References**: [**1**] Abbott et al. (2019a); [**4**] Abbott et al. (2021); [**10**] Abbott et al. (2020a).

	GW event	D_L (Mpc)	L_{peak} ($\times 10^{56}$ erg s^{-1})	z	M_{rad} ($M_\odot$)	Ref.
1	GW150914	440^{+150}_{-170}	$3.6^{+0.4}_{-0.4}$	$0.09^{+0.03}_{-0.03}$	$3.1^{+0.4}_{-0.4}$	[1]
2	GW151012	1080^{+550}_{-490}	$3.2^{+0.8}_{-1.7}$	$0.21^{+0.09}_{-0.09}$	$1.6^{+0.6}_{-0.5}$	[1]
3	GW151226	450^{+180}_{-190}	$3.4^{+0.7}_{-1.7}$	$0.09^{+0.04}_{-0.04}$	$1.0^{+0.1}_{-0.2}$	[1]
4	GW170104	990^{+440}_{-430}	$3.3^{+0.6}_{-1.0}$	$0.20^{+0.08}_{-0.08}$	$2.2^{+0.5}_{-0.5}$	[1]
5	GW170608	320^{+120}_{-110}	$3.5^{+0.4}_{-1.3}$	$0.07^{+0.02}_{-0.02}$	$0.9^{+0.0}_{-0.1}$	[1]
6	GW170729	2840^{+1400}_{-1360}	$4.2^{+0.9}_{-1.5}$	$0.49^{+0.19}_{-0.21}$	$4.8^{+1.7}_{-1.7}$	[1]
7	GW170809	1030^{+320}_{-390}	$3.5^{+0.6}_{-0.9}$	$0.20^{+0.05}_{-0.07}$	$2.7^{+0.6}_{-0.6}$	[1]
8	GW170814	600^{+150}_{-220}	$3.7^{+0.4}_{-0.5}$	$0.12^{+0.03}_{-0.04}$	$2.7^{+0.4}_{-0.3}$	[1]
9	GW170818	1060^{+420}_{-380}	$3.4^{+0.5}_{-0.7}$	$0.21^{+0.07}_{-0.07}$	$2.7^{+0.5}_{-0.5}$	[1]
10	GW170823	1940^{+970}_{-900}	$3.6^{+0.7}_{-1.1}$	$0.35^{+0.15}_{-0.15}$	$3.3^{+1.0}_{-0.9}$	[1]
11	GW190408_181802	1550^{+400}_{-600}		$0.29^{+0.06}_{-0.10}$	1.9±0.7*	[4]
12	GW190412	740^{+140}_{-170}		$0.15^{+0.03}_{-0.03}$	1.1±0.4*	[4]
13	GW190413_052954	3550^{+2270}_{-1660}		$0.59^{+0.29}_{-0.24}$	2.6±1.0*	[4]
14	GW190413_134308	4450^{+2480}_{-2120}		$0.71^{+0.31}_{-0.30}$	3.3±1.2*	[4]
15	GW190421_213856	2880^{+1370}_{-1380}		$0.49^{+0.19}_{-0.21}$	3.2±1.2*	[4]

(continues on next page)

Table 3 (continued).

	GW event	D_L (Mpc)	L_{peak} ($\times 10^{56}$ erg s^{-1})	z	M_{rad} ($M_\odot$)	Ref.
16	GW190424_180648	2200^{+1580}_{-1160}		$0.39^{+0.23}_{-0.19}$	3.7±1.4*	[4]
17	GW190425	160^{+70}_{-70}				[4]
18	GW190503_185404	1450^{+690}_{-630}		$0.27^{+0.11}_{-0.11}$	3.1±1.2*	[4]
19	GW190512_180714	1430^{+550}_{-550}		$0.27^{+0.09}_{-0.10}$	1.4±0.5*	[4]
20	GW190513_205428	2060^{+880}_{-800}		$0.37^{+0.13}_{-0.13}$	2.3±0.9*	[4]
21	GW190514_065416	4130^{+2650}_{-2170}		$0.67^{+0.33}_{-0.31}$	2.7±1.0*	[4]
22	GW190517_055101	1860^{+1620}_{-840}		$0.34^{+0.24}_{-0.14}$	4.2±1.6*	[4]
23	GW190519_153544	2530^{+1830}_{-920}		$0.44^{+0.24}_{-0.14}$	5.6±2.1*	[4]
24	GW190521	3920^{+2190}_{-1950}		$0.64^{+0.28}_{-0.28}$	7.6±2.9*	[4]
25	GW190521_074359	1240^{+400}_{-570}		$0.24^{+0.07}_{-0.10}$	3.7±1.4*	[4]
26	GW190527_092055	2490^{+2480}_{-1240}		$0.44^{+0.34}_{-0.20}$	2.7±1.0*	[4]
27	GW190602_175927	2690^{+1790}_{-1120}		$0.47^{+0.25}_{-0.17}$	5.4±2.0*	[4]
28	GW190620_030421	2810^{+1680}_{-1310}		$0.49^{+0.23}_{-0.20}$	4.9±1.8*	[4]
29	GW190630_185205	890^{+560}_{-370}		$0.18^{+0.10}_{-0.07}$	2.7±1.0*	[4]
30	GW190701_203306	2060^{+760}_{-730}		$0.37^{+0.11}_{-0.12}$	4.1±1.5*	[4]
31	GW190706_222641	4420^{+2590}_{-1930}		$0.71^{+0.32}_{-0.27}$	5.1±1.9*	[4]
32	GW190707_093326	770^{+380}_{-370}		$0.16^{+0.07}_{-0.07}$	0.9±0.3*	[4]

(continues on next page)

Table 3 (continued).

	GW event	D_L (Mpc)	L_{peak} ($\times 10^{56}$ erg s^{-1})	z	M_{rad} ($M_\odot$)	Ref.
33	GW190708_232457	880^{+330}_{-390}		$0.18^{+0.06}_{-0.07}$	1.4±0.5*	[4]
34	GW190719_215514	3940^{+2590}_{-2000}		$0.64^{+0.33}_{-0.29}$	2.9±1.1*	[4]
35	GW190720_000836	790^{+690}_{-320}		$0.16^{+0.12}_{-0.06}$	1.1±0.4*	[4]
36	GW190727_060333	3300^{+1540}_{-1500}		$0.55^{+0.21}_{-0.22}$	3.3±1.2*	[4]
37	GW190728_064510	870^{+260}_{-370}		$0.18^{+0.05}_{-0.07}$	1.0±0.4*	[4]
38	GW190731_140936	3300^{+2390}_{-1720}		$0.55^{+0.31}_{-0.26}$	3.1±1.2*	[4]
39	GW190803_022701	3270^{1950}_{-1580}		$0.55^{+0.26}_{-0.24}$	2.8±1.1*	[4]
40	GW190814	241^{+41}_{-45}		$0.053^{+0.009}_{-0.010}$	0.2±0.1*	[10]
41	GW190828_063405	2130^{+660}_{-930}		$0.38^{+0.10}_{-0.15}$	3.1±1.2*	[4]
42	GW190828_065509	1600^{+620}_{-600}		$0.30^{+0.10}_{-0.10}$	1.3±0.5*	[4]
43	GW190909_114149	3770^{+3270}_{-2220}		$0.62^{+0.41}_{-0.33}$	3.0±1.1*	[4]
44	GW190910_112807	1460^{+1030}_{-580}		$0.28^{+0.16}_{-0.10}$	3.8±1.4*	[4]
45	GW190915_235702	1620^{+710}_{-610}		$0.30^{+0.11}_{-0.10}$	2.7±1.0*	[4]
46	GW190924_021846	570^{+220}_{-220}		$0.12^{+0.04}_{-0.04}$	0.6±0.2*	[4]
47	GW190929_012149	2130^{+3650}_{-1050}		$0.38^{+0.49}_{-0.17}$	2.8±1.1*	[4]
48	GW190930_133541	760^{+360}_{-320}		$0.15^{+0.06}_{-0.06}$	0.9±0.3*	[4]

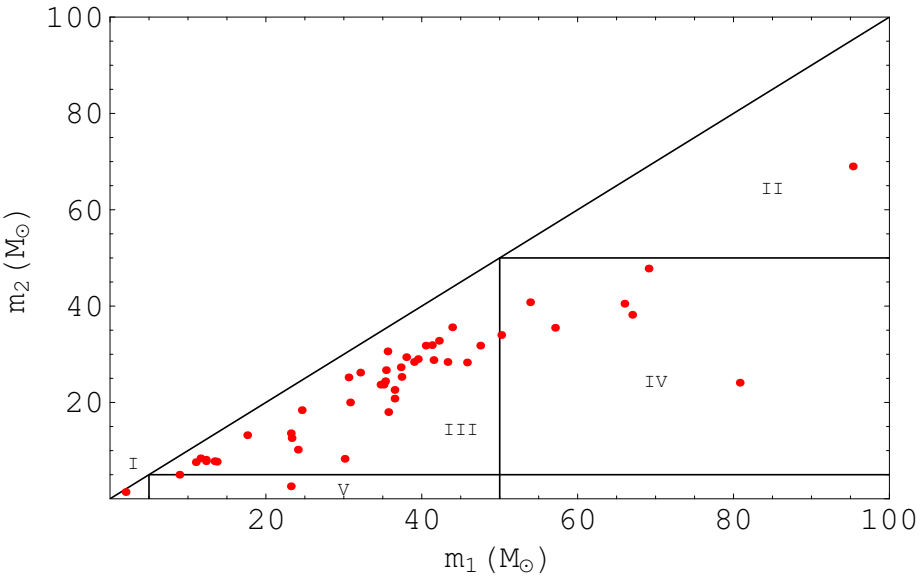

Figure 4: The relation between the masses m_1 and m_2 ($m_1 \geq m_2$) for the 48 BBHs shown on Table 1. The plane is divided into five regions: I) lower mass gap; II) upper mass gap; III) typical stellar evolution region; IV and V) hybrid regions (see text for more details).

the spin of the secondary BH, a_2. Although the number of cases is small, there seems to be a tendency for the secondary BH (less massive one) to possess an higher spin with respect to the primary BH. This tendency could also be somehow observed in Figures 8 and 9.

In Figure 10 we plot the final mass M_f against the total mass M (equation 1) for the 48 BBHs shown in Table 1. We performed a linear regression (using the Least Squares Method) from which we obtained the relation:

$$M_f \approx 0.95M + 0.16 \tag{26}$$

Observing that the intercept point at $M = 0$ is $\sim 10^{-1} M_\odot$ we will just consider:

$$M_f \approx 0.95M \tag{27}$$

In Figures 11 and 12 we plot, respectively, the radiated mass M_{rad} against the total mass M and the final mass M_f using the values from Tables 1 and 3. In both cases we performed a linear regression obtaining:

$$M_{rad} \approx 0.0478M \tag{28}$$

$$M_{rad} \approx 0.0497M_f \tag{29}$$

With the help of equation (25) we recover from both equations (28) and (29), once again, the relation given in equation (27). This allows us to conclude that

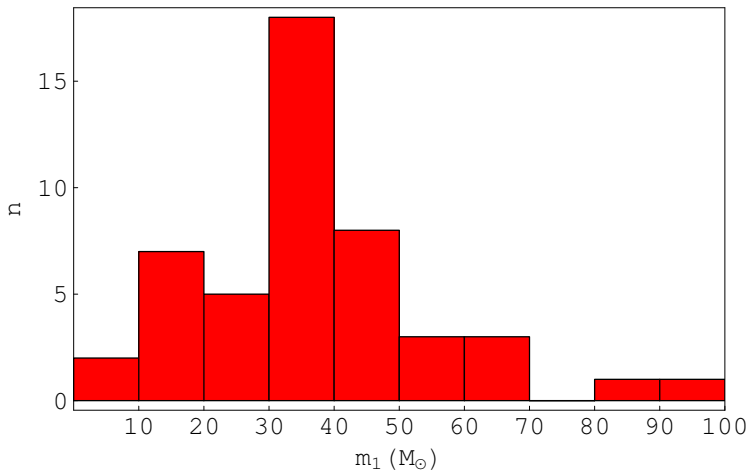

Figure 5: Distribution of the masses m_1 shown on Table 1. There are 18 (37.5%) primary BHs with masses between 30-40 $M_\odot$.

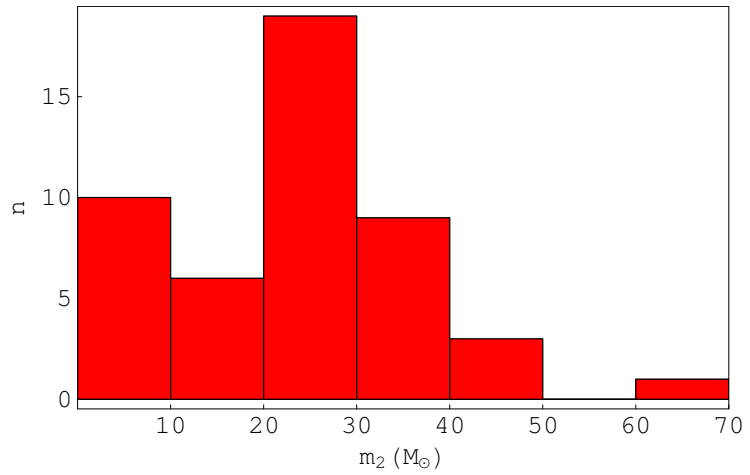

Figure 6: Distribution of the masses m_2 shown on Table 1. There are 19 ($\approx$ 38.6%) secondary BHs with masses between 20-30 $M_\odot$.

in average in a BBH merger event a total of $\approx 5\%$ of the initial mass is converted into energy.

Notice, however, that the Least Squares Method requires that the independent variable is known with great precision, which is not the case in either of our examples (e.g., on the case of GW170729 we have for a mass of $79.5M_\odot$ associated errors higher than $10M_\odot$, cf. Table 1). This means that when dealing with the result given by expression (27) we must keep this in mind and be precocious.

In Figures 13 and 14 we can see the distribution of the total mass M and of the final mass M_f, respectively.

Using equations (27) and (28) we can calculate the final mass M_f and the

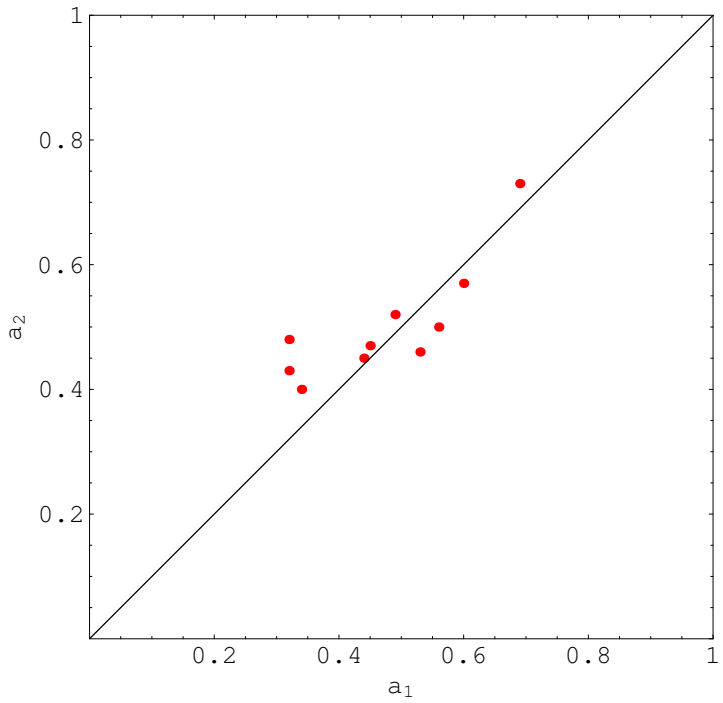

Figure 7: Relation between the spin of the primary BH, a_1, and the spin of the secondary BH, a_2. The values are shown on Table 2. The solid line represents the identity function.

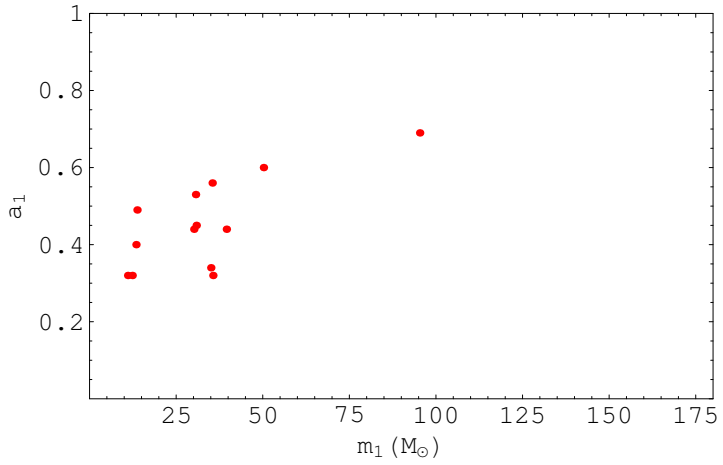

Figure 8: Relation between the primary mass, m_1, and the primary spin, a_1. Values are shown on Table 1 and on Table 2, respectively.

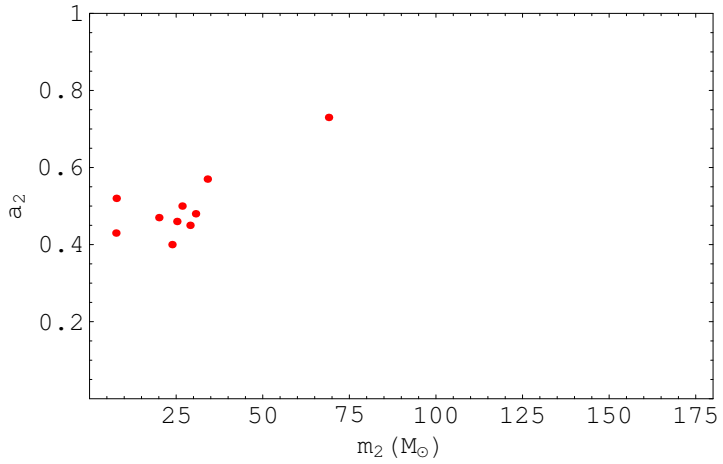

Figure 9: Relation between the secondary mass, m_2, and the secondary spin, m_2. Values are shown on Table 1 and on Table 2, respectively.

radiated energy M_{rad} of the event GW190425, which values were missing from Table 1. We get that $M_f \approx 3.23 M_\odot$ and $M_{rad} \approx 0.16 M_\odot$.

In order to analyse some kind of dependence between the values of the final spin a_f and the parameters of total mass M, final mass M_f, radiated energy M_{rad} and mass ratio q, we plotted Figures 15, 16, 17 and 18. In these 4 figures we noted that the value of a_f is approximately constant if we did not consider the outlier present in the plots, GW190814. Therefore, we calculated the mean value of a_f and also the standard deviation, such that:

$$a_f \approx 0.70 \pm 0.04 \tag{30}$$

In Figure 19 we represent the relation between the effective inspiral spin (χ_{eff}) and the effective precession spin (χ_p) for the events known to date shown on Table 2. We get that 85% of the events has χ_{eff} between -0.2 and 0.2 and that there are 6 events that are outside of that region (GW170729, GW190412, GW190517_055101, GW190519_153544, GW190620_030421, GW190706_222641). In Figures 21 and 20 we represented the distribution of χ_{eff} and χ_p, respectively.

5 Conclusions

The first direct GW detection was made by LIGO on September 14, 2015. This event, designated as GW150914, was originated when two BHs with, respectively, $35.6 M_\odot$ and $30.6 M_\odot$, inspiraling in a BBH system merged given rise to a single BH with $63.1 M_\odot$. As a result an amount of $\approx 3.1 M_\odot$ was radiated into space mainly in the form of GWs. Since then Advanced LIGO and Advanced Virgo have detected dozens of GW events. Here we focused on the 48 GW events associated with the merge of BBHs that were detected until now.

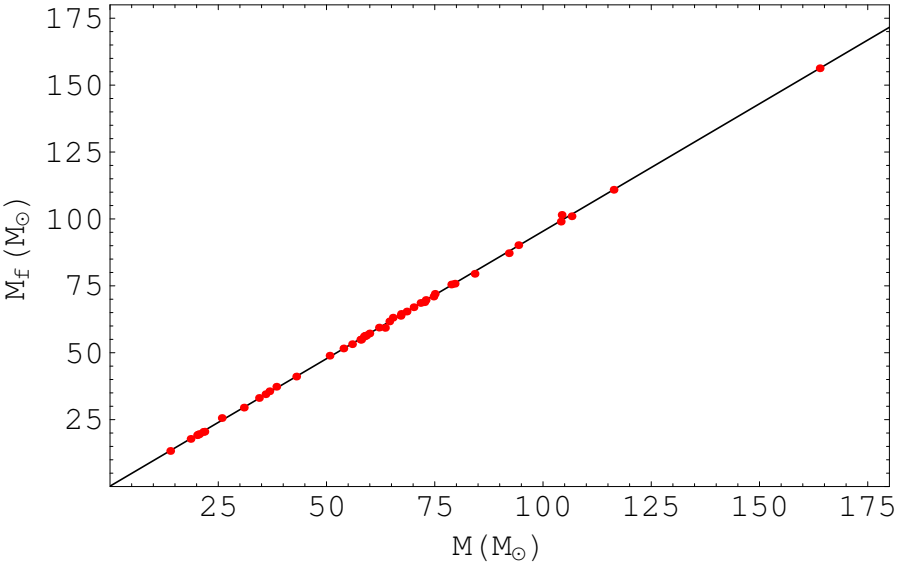

Figure 10: The relation between the total masses, M, and the final masses, M_f, for the 48 BBHs shown on Table 1.The solid line was obtained by linear regression (see equation (27) and text for more details).

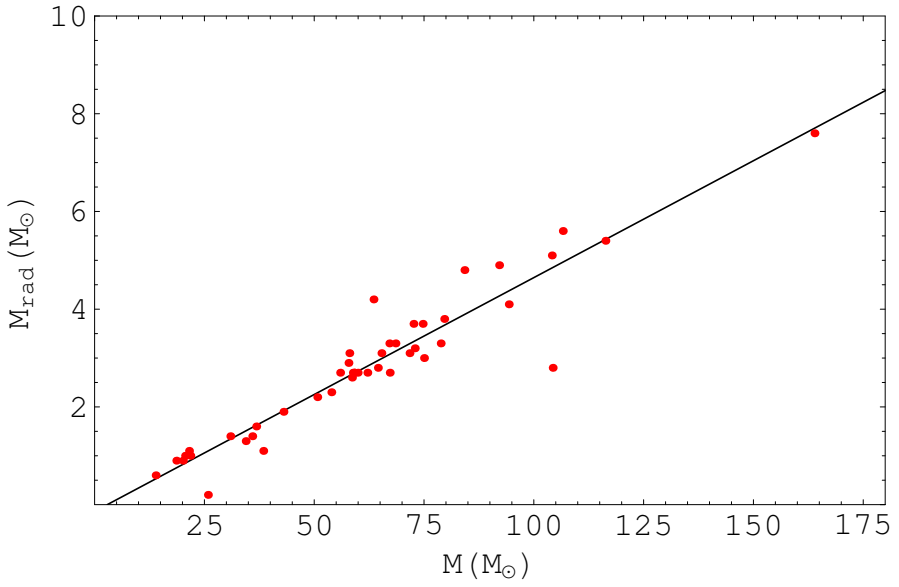

Figure 11: Relation between the total mass, M, and the radiated energy, M_{rad}. Values are shown on Table 1 and on Table 3, respectively. The solid line was obtained by linear regression (see equation (28) and text for more details).

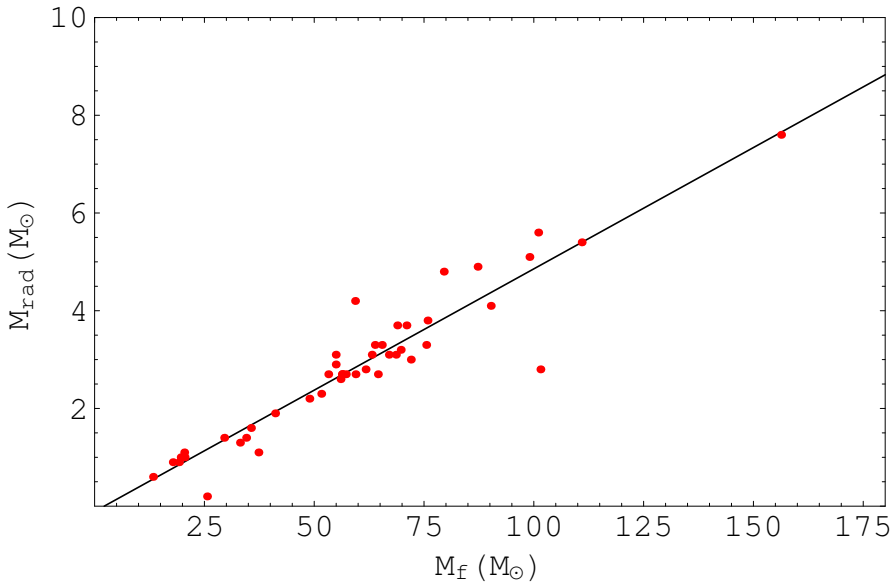

Figure 12: Relation between the final mass, M_f, and the radiated energy, M_{rad}. Values are shown on Table 1 and on Table 3, respectively. The solid line was obtained by linear regression (see equation (29) and text for more details).

In Tables 1, 2 and 3 we summarize some of the key parameters that characterize these 48 BBH systems.

In Table 1 we compiled the parameters related with the mass of each of the individual BHs or with the mass of the final BH. Namely we have m_1 (the mass of the primary BH), m_2 (the mass of the secondary BH; conventionally $m_2 \leq m_1$), M (the system total mass, equation 1), M_{chirp} (cf. equations 12 and 13), M_f (final mass) and q (mass ratio, equation 3).

In Table 2 we compiled the parameters related with the spin of each of the individual BHs. Namely we have a_1 (the spin of the primary BH), a_2 (the spin of the secondary BH), χ_{eff} (the effective inspiral spin, equation 16), χ_p (the effective precession spin, equation 18) and a_f (the spin of the final BH, equation 21).

Finally, Table 3 was dedicated to the parameters related to energy and distance. Namely we have D_L (the luminosity distance, equation 23), L_{peak} (the luminosity peak), z (the cosmological redshift) and M_{rad} (the readiated energy, equation 25).

We were unable to find the values for all the parameters in the literature. In particular in the case of the mass ratio q we only found the values corresponding to the events GW190412 and GW190814, so we determined the remaining 46 values using equation (3). In the case of M_{rad} we had values for only the first 10 events, corresponding to the BBH mergers detected during the first two observing runs (O1 and O2). We managed to determine the values for the rest of the events using equation (25) (see Section 3 for details).

In Tables 2 and 3 we were also unable to find all the values in the litera-

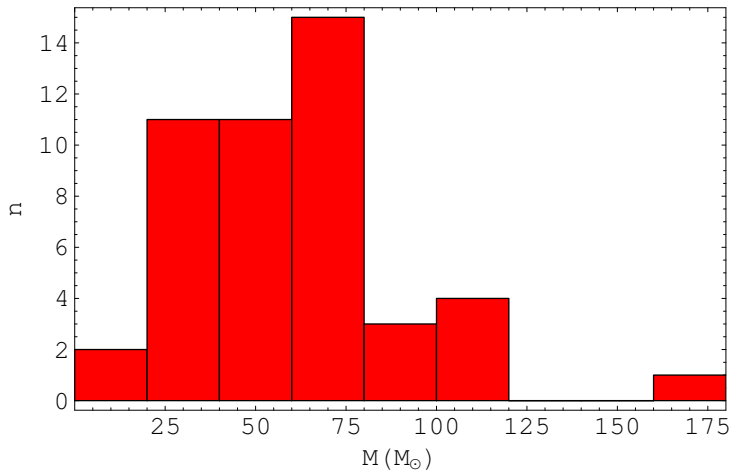

Figure 13: Distribution of the masses M shown on Table 1. 16 out of the 48 BBHs on this paper has total mass between 60-80 $M_{\odot}$.

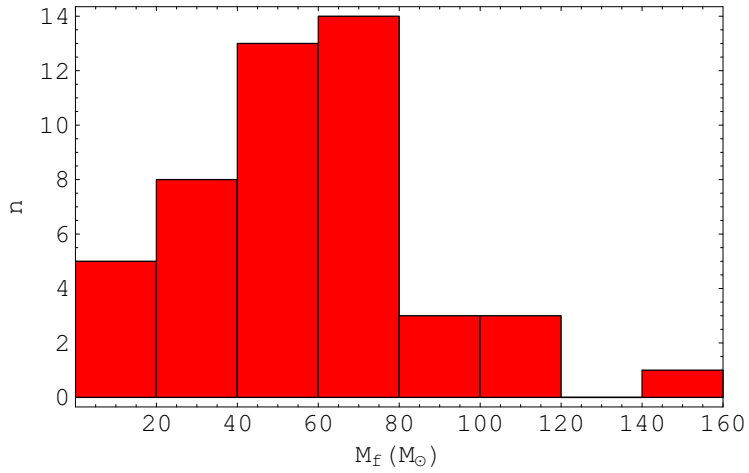

Figure 14: Distribution of the masses M_f shown on Table 1. 14 out of the 48 BBHs has final mass between 40-80 $M_{\odot}$.

ture. In Table 2 we only found values of a_1 for 13 events and values of a_2 for 10 events. There are also three values of χ_p (GW190425, GW190719_215514 and GW190909_114149) and one value of a_f (GW190425) that are missing in the literature. In Table 3 we could only find values of L_{peak} for the first 10 events, corresponding to the BBH mergers detected during the first two observing runs (O1 and 02) (see Section 3 for details).

An open and controversial question related to the existence of these BBH systems is related to their true origin, more exactly, if they are the result of standard stellar evolution or if they were originated in the primordial Universe long before the first stars.

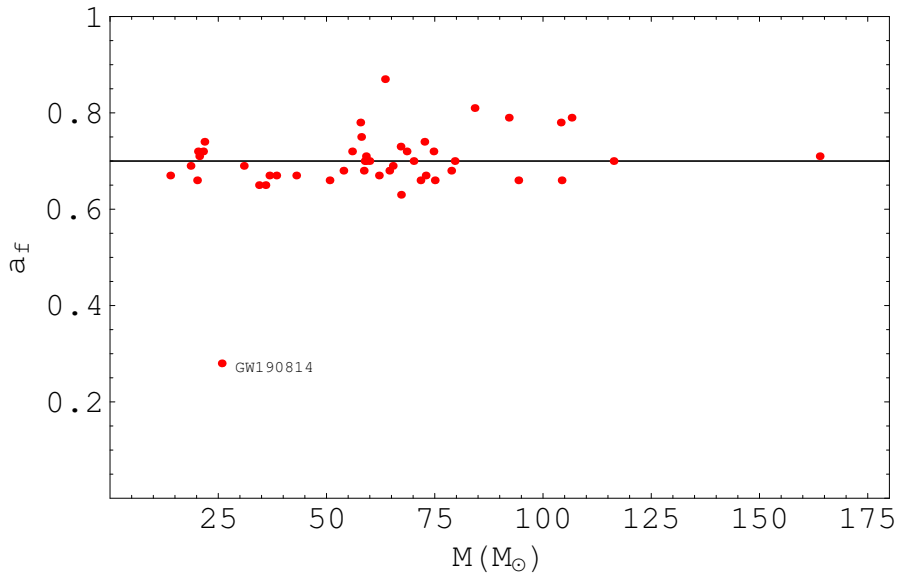

Figure 15: Relation between the total mass, M, and the spin of the final BH, a_f. Values are shown on Table 1 and on Table 2, respectively. The horizontal straight line represents the mean value of a_f if we do not consider GW190814.

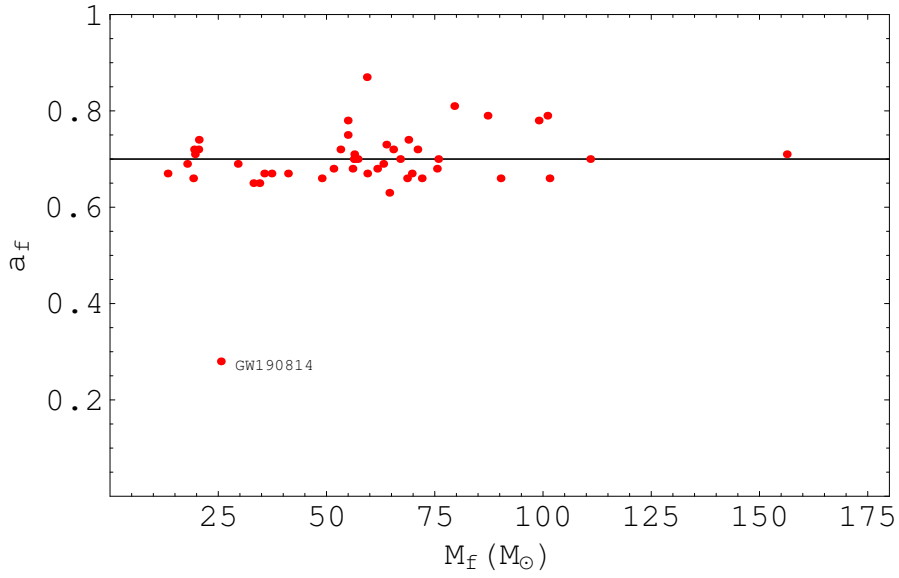

Figure 16: Relation between the final mass, M_f, and the final spin, a_f, shown on Table 1 and on Table 2, respectively. The horizontal straight line represents the mean value of a_f if we do not consider GW190814.

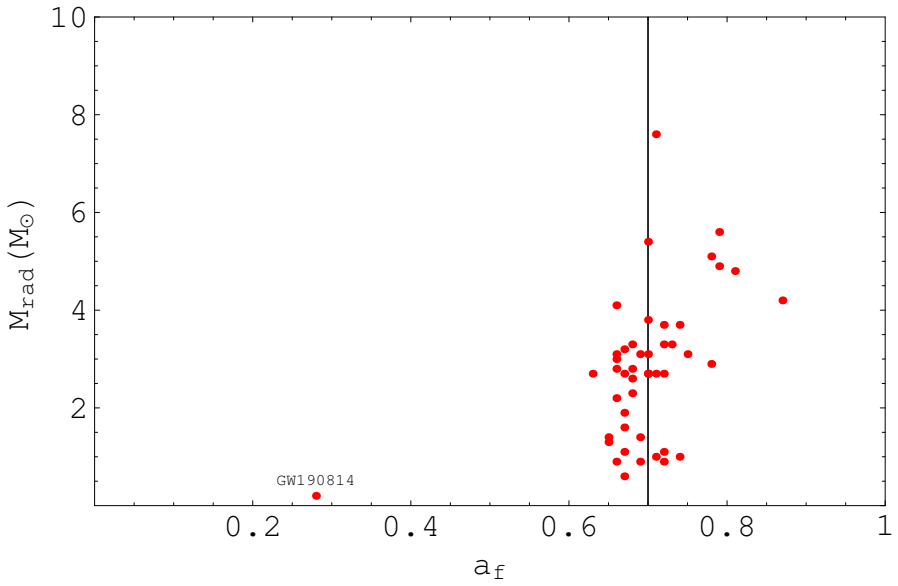

Figure 17: Relation between the spin of the final BH, a_f, and the radiated energy, M_{rad}. Values are shown on Table 2 and on Table 3, respectively. The vertical straight line represents the mean value of a_f if we do not consider GW190814.

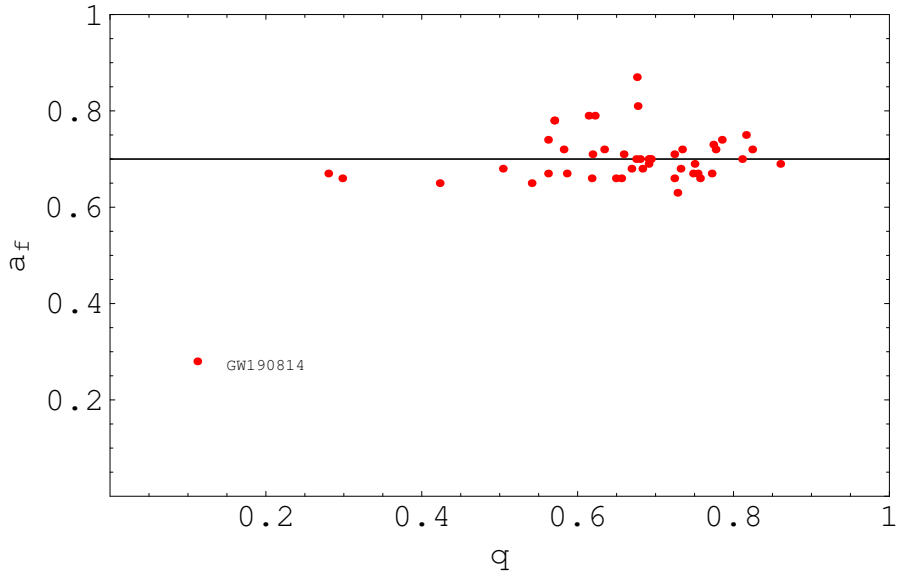

Figure 18: Relation between the mass ratio, q, and the spin of the final BH, a_f. Values are shown on Table 1 and on Table 2, respectively. The horizontal straight line represents the mean value of a_f if we do not consider GW190814.

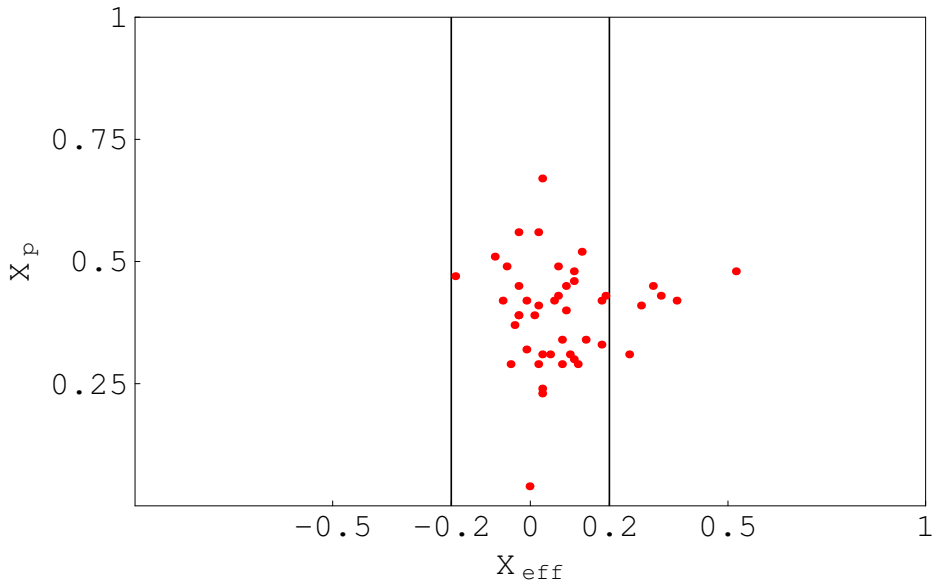

Figure 19: Relation between the effective inspiral spin, χ_{eff}, and the effective precession spin, χ_p, shown on Table 2. The values between the two vertical lines on $\chi_{eff} = -0.2$ and $\chi_{eff} = 0.2$ represent 85% of the events.

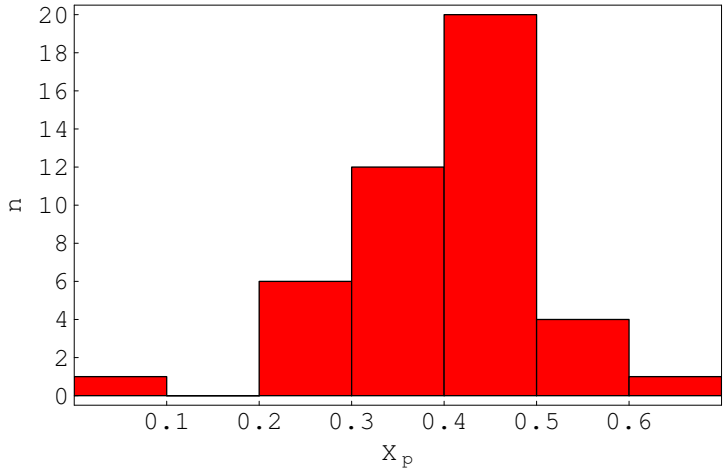

Figure 20: Distribution of the values of the effective precession spin, χ_p, of the 48 BBHs events presented in this paper. Values are shown on Table 2. There is a large percentage ($\approx 41.67\%$) of events with values of χ_p between 0.4 and 0.5.

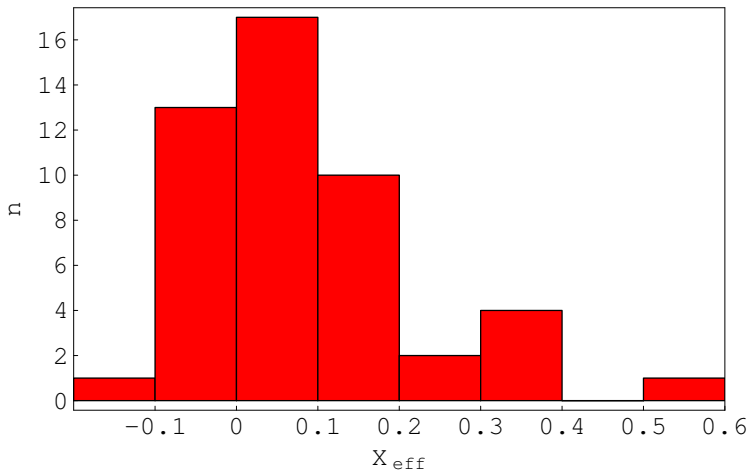

Figure 21: Distribution of the values of the effective inspiral spin, χ_{eff}, of the 48 BBHs events presented in this paper. Values are shown on Table 2. 85% of the events have values of χ_{eff} between -0.2 and 0.2.

BHs with masses larger than $\sim 50M_{\odot}$ are not common among the observed BH candidates known to date. The same goes to BHs with masses smaller than $\sim 5M_{\odot}$. On the other hand we could have PBHs with almost all kinds of masses, depending on the considered models. With this idea on mind we divided the (m_1, m_2) plane into five different regions (cf. Figure 4).

In Region I, which corresponds to the lower mass gap, we have a single event: GW190425 ($m_1 = 2.0M_{\odot}$ and $m_2 = 1.4M_{\odot}$) and in Region II, which corresponds to the upper mass gap, we have also a single event: GW190521 ($m_1 = 95.3M_{\odot}$ and $m_2 = 69.0M_{\odot}$). In region V we have the case GW190814 with $m_2 = 2.59M_{\odot}$ which fits the lower mass gap and $m_1 = 23.2M_{\odot}$ which does not fit the lower mass gap (region V can be seen as an hybrid region). All these three BBHs are, according to their masses, potentially of primordial origin. This issue was already pointed out by Clesse & Garcia-Bellido (2020) as systems composed of PBHs formed during the QCD epoch.

Besides region V we have yet another hybrig region in Figure 4. In fact, in region IV we have seven BBHs (GW170729, GW190519_153544, GW190602_175927, GW190620_030421, GW190701_203306, GW190706_222641, GW190929_012149) for which although m_1 fits the upper mass gap, m_2 does not (see Table 1 for the mass values). It is reasonable to at least consider the hypothesis that these BBHs are also potentially of primordial origin. Another scenario is that we are in the presence of BBHs formed after an encounter of a PBH with a BH of stellar origin (although this is not impossible it seems highly unlikely).

On the other hand the BBHs located within region III (see Figure 4), in fact the majority of the 48 BBHs on our list, are those which existence is in accordance with typical stellar evolution (although they could be also of primordial origin).

Table 4: 10 BBHs of primordial origin, values of m_1, m_2 and χ_{eff} from Tables 1 and 2.

GW event	$m_1(M_\odot)$	$m_2(M_\odot)$	χ_{eff}
GW170729	$50.2^{+16.2}_{-10.2}$	$34.0^{+9.1}_{-10.1}$	$0.37^{+0.21}_{-0.25}$
GW190425	$2.0^{+0.6}_{-0.3}$	$1.4^{+0.3}_{-0.3}$	$0.06^{+0.11}_{-0.05}$
GW190519_153544	$66.0^{+10.7}_{-12.0}$	$40.5^{+11.0}_{-11.1}$	$0.31^{+0.20}_{-0.22}$
GW190521	$95.3^{+28.7}_{-18.9}$	$69.0^{+22.7}_{-23.1}$	$0.03^{+0.32}_{-0.39}$
GW190602_175927	$69.1^{+15.7}_{-13.0}$	$47.8^{+14.3}_{-17.4}$	$0.07^{+0.25}_{-0.24}$
GW190620_030421	$57.1^{+16.0}_{-12.7}$	$35.5^{+12.2}_{-12.3}$	$0.33^{+0.22}_{-0.25}$
GW190701_203306	$53.9^{+11.8}_{-8.0}$	$40.8^{+8.7}_{-12.0}$	$-0.07^{+0.23}_{-0.29}$
GW190706_222641	$67.0^{+14.6}_{-16.2}$	$38.2^{+14.6}_{-13.3}$	$0.28^{+0.26}_{-0.29}$
GW190814	$23.2^{+1.1}_{-1.0}$	$2.59^{+0.08}_{-0.09}$	$-0.002^{+0.060}_{-0.061}$
GW190929_012149	$80.8^{+33.0}_{-33.2}$	$24.1^{+19.3}_{-10.6}$	$0.01^{+0.34}_{-0.33}$

In Figure 4 we have seven events that are present in region IV and comparing these events with those present in Figure 19 that are outside of the region between the vertical lines ($\chi_{eff} = -0.2$ and $\chi_{eff} = 0.2$), we get four events in common (GW170729, GW190519_153544, GW190620_030421 and GW190706_222641). The events that are not in common are GW190412, GW190517_055101 (from Figure 19), GW190602_175927, GW190701_203306 and GW190929_012149 (from the region IV in Figure 4).

In summary we have:

- Regions I, II, IV and V: 10 BBHs of primordial origin (see Table 4)
- Region II: 38 BBHs of stellar (or primordial origin)

In Figures 5 and 6 we have shown the distribution of m_1 and m_2, respectively. The masses of the 96 individual BHs are mostly within the range $[20M_\odot, 40M_\odot]$ which is in agreement with some scenarios of PBH formation (see e.g. Sobrinho & Augusto (2020)).

By linear regression (see Figures 10, 11 and 12) we obtained the relation $M_f \approx 0.95M$ (equation 27). This allowed us to determine the value of M_f for the event GW190425, which was missing from Table 1, such that $M_f = 3.23M_\odot$. By linear regression we also obtained the relation $M_{rad} \approx 0.0478M$ (equation 28), such that this allowed us to determine the value of M_{rad} for the event GW190425, which was also missing from Table 3, $M_{rad} = 0.16M_\odot$.

We noticed that with the available data the final spin of the resulting BH is almost constant $a_f \approx 0.70 \pm 0.04$ (see Figures 15, 16, 17 and 18) if we do not consider the outlier event GW190814.

In terms of future work, it is intended to complete the sets of parameters presented in the tables, either with observational data or with theoretically determined values, as well as to explore the connection between the observed events and their eventual primordial origin.

References

Abbott, B. P., Abbott, R., Abbott, T. D., et al. 2020, *GW190425: Observation of a Compact Binary Coalescence with Total Mass* $\sim 3.4M_{\odot}$, ApJL, 892, L3. doi:10.3847/2041-8213/ab75f5

Abbott, B. P., Abbott, R., Abbott, T. D., et al. 2019a, *GWTC-1: A Gravitational-Wave Transient Catalog of Compact Binary Mergers Observed by LIGO and Virgo during the First and Second Observing Runs*, Physical Review X, 9, 031040 [arXiv:1811.12907]

Abbott, B. P., Abbott, R., Abbott, T. D., et al. 2019b, *Binary Black Hole Population Properties Inferred from the First and Second Observing Runs of Advanced LIGO and Advanced Virgo*, ApJL, 882, L24. doi:10.3847/2041-8213/ab3800

Abbott, B. P., Abbott, R., Abbott, T. D., et al. 2017a, *GW170814: A Three-Detector Observation of Gravitational Waves from a Binary Black Hole Coalescence*, PhRvL, 19, 141101, [arXiv:1709.09660]

Abbott, B. P., Abbott, R., Abbott, T. D., et al. 2017b, *GW170104: Observation of a 50-Solar-Mass Binary Black Hole Coalescence at Redshift 0.2*, PhRvL, 118, 221101 [arXiv:1706.01812]

Abbott, B. P., Abbott, R., Abbott, T. D., et al. 2017c, *The basic physics of the binary black hole merger GW150914*, Annalen der Physik, 529, 1600209.

Abbott, B. P., Abbott, R., Abbott, T. D., et al. 2016a, *Binary Black Hole Mergers in the First Advanced LIGO Observing Run*, Physical Review X, 6, 041015 [arXiv:1606.04856]

Abbott, B. P., Abbott, R., Abbott, T. D., et al. 2016b, *Properties of the Binary Black Hole Merger GW150914*, PhRvL, 116, 241102 [arXiv:1602.03840]

Abbott, B. P., Abbott, R., Abbott, T. D., et al. 2016c, *Observation of Gravitational Waves from a Binary Black Hole Merger*, PhRvL, 116, 061102. doi:10.1103/PhysRevLett.116.061102

Abbott, B. P., Abbott, R., Abbott, T. D., et al. 2016d, *Astrophysical Implications of the Binary Black-hole Merger GW150914*, ApJL, 818, L22. doi:10.3847/2041-8205/818/2/L22

Abbott, R., Abbott, T. D., Abraham, S., et al. 2021, *GWTC-2: Compact Binary Coalescences Observed by LIGO and Virgo during the First Half of the Third Observing Run*, Physical Review X, 11, 021053 [arXiv:2010.14527]

Abbott, R., Abbott, T. D., Abraham, S., et al. 2020a, *GW190814: Gravitational Waves from the Coalescence of a 23$M_\odot$ Black Hole with a 2.6$M_\odot$ Compact Object*, ApJL, 896, L44, [arXiv:2006.12611]

Abbott, R., Abbott, T. D., Abraham, S., et al. 2020b, *GW190521: A Binary Black Hole Merger with a Total Mass of 150$M_\odot$*, PhRvL, 125, 101102 [arXiv:2009.01075]

Baumgarte, T. W. & Shapiro, S. L., 2010, *Numerical Relativity: Solving Einstein's Equations on the Computer*, Cambridge University Press, ISBN: 9780521514071.

Baumgarte, T. W. & Shapiro, S. L., 2011, *Binary Black Hole Mergers*, Physics Today, 64, 32.

Belczynski, K., Klencki, J., Fields, C. E., et al. 2020, *Evolutionary roads leading to low effective spins, high black hole masses, and O1/O2 rates for LIGO/Virgo binary black holes*, AAP, 636, A104. doi:10.1051/0004-6361/201936528

Belotsky K. M., Dokuchaev V. I., Eroshenko Y. N., Esipova E. A., Khlopov M. Y., Khromykh L. A., Kirillov A. A., et al., 2019, *Clusters of Primordial Black Holes*, EPJC, 79, 246. doi:10.1140/epjc/s10052-019-6741-4

Bird S., Cholis I., Muñoz J. B., Ali-Haïmoud Y., Kamionkowski M., Kovetz E. D., Raccanelli A., et al., 2016, *Did LIGO Detect Dark Matter?*, PhRvL, 116, 201301. doi:10.1103/PhysRevLett.116.201301

Blinnikov, S., Dolgov, A., Porayko, N. K., et al. 2016, *Solving puzzles of GW150914 by primordial black holes*, JCAP, 2016, 036. doi:10.1088/1475-7516/2016/11/036

Buonanno, A., Kidder, L. E., & Lehner, L. 2008, *Estimating the final spin of a binary black hole coalescence*, PhRvD, 77, 026004 [arXiv:0709.3839]

Clesse, S. & Garcia-Bellido, J. 2020, *GW190425, GW190521 and GW190814: Three candidate mergers of primordial black holes from the QCD epoch*, arXiv:2007.06481

Clesse, S. & García-Bellido, J. 2017, *The clustering of massive Primordial Black Holes as Dark Matter: Measuring their mass distribution with advanced LIGO*, Physics of the Dark Universe, 15, 142. doi:10.1016/j.dark.2016.10.002

Cromartie, H. T., Fonseca, E., Ransom, S. M., et al. 2020, *Relativistic Shapiro delay measurements of an extremely massive millisecond pulsar*, Nature Astronomy, 4, 72. doi:10.1038/s41550-019-0880-2

Cutler, C. & Flanagan, É. E. 1994, *Gravitational waves from merging compact binaries: How accurately can one extract the binary's parameters from the inspiral waveform?*, PhRvD, 49, 2658. doi:10.1103/PhysRevD.49.2658

De, S., Biwer, C. M., Capano, C. D., et al. 2019, *Posterior samples of the parameters of binary black holes from Advanced LIGO, Virgo's second observing run*, Scientific Data, 6, 81 [arXiv:1811.09232v3]

d'Inverno R., 1993, *Introducing Einstein's relativity*, Oxford, Claredon Press.

De Luca, V., Franciolini, G., Pani, P., et al. 2020, *The evolution of primordial black holes and their final observable spins*, JCAP, 2020, 052. doi:10.1088/1475-7516/2020/04/052

Fanizza, G., Franchini, G., Gasperini, M., et al. 2020, *Comparing the luminosity distance for gravitational waves and electromagnetic signals in a simple model of quadratic gravity*, General Relativity and Gravitation, 52, 111. doi:10.1007/s10714-020-02760-5

Farr, W. M., Stevenson, S., Miller, M. C., et al. 2017, *Distinguishing Spin-Aligned and Isotropic Black Hole Populations With Gravitational Waves*, Nature, 548, 426 [arXiv:1706.01385]

Farr, B., Berry, C. P. L., Farr, W. M., et al. 2016, *Parameter Estimation on Gravitational Waves from Neutron-star Binaries with Spinning Components*, ApJ, 825, 116 [arXiv:1508.05336]

Fernandez, N. & Profumo, S. 2019, *Unraveling the origin of black holes from effective spin measurements with LIGO-Virgo*, JCAP, 2019, 022. doi:10.1088/1475-7516/2019/08/022

Gerosa, D., Mould, M., Gangardt, D., et al. 2021, *A generalized precession parameter χ_p to interpret gravitational-wave data*, PhRvD, 103, 064067. doi:10.1103/PhysRevD.103.064067

Gow A. D., Byrnes C. T., Hall A., Peacock J. A., 2020, *Primordial black hole merger rates: distributions for multiple LIGO observables*, JCAP, 2020, 031. doi:10.1088/1475-7516/2020/01/031

Hogg, D. W. 1999, *Distance measures in cosmology*, astro-ph/9905116

Kenyon, I. R. 1990, *General relativity.*, by Kenyon, I. R.. Oxford University Press, Oxford (UK), 1990, 241 p., ISBN 0-19-851995-8.

Kohri, K. & Terada, T. 2018, *Primordial black hole dark matter and LIGO/Virgo merger rate from inflation with running spectral indices: formation in the matter- and/or radiation-dominated universe*, Classical and Quantum Gravity, 35, 235017. doi:10.1088/1361-6382/aaea18

Landau, L. D. & Lifshitz, E. M. 1969, Course of Theoretical Physics, Oxford: Pergamon Press, 1969, 2nd ed.

Özel, F. & Freire, P. 2016, *Masses, Radii, and the Equation of State of Neutron Stars* , ARA&A, 54, 401. doi:10.1146/annurev-astro-081915-023322

Sasaki, M., Suyama, T., Tanaka, T., et al. 2018, *Primordial black holes-perspectives in gravitational wave astronomy*, Classical and Quantum Gravity, 35, 063001. doi:10.1088/1361-6382/aaa7b4

Scelfo, G., Bellomo, N., Raccanelli, A., et al. 2018, *GWxLSS: chasing the progenitors of merging binary black holes*, JCAP, 2018, 039. doi:10.1088/1475-7516/2018/09/039

Schmidt, P., Ohme, F., & Hannam, M. 2015, *Towards models of gravitational waveforms from generic binaries II: Modelling precession effects with a single effective precession parameter*, PhRvD, 91, 024043 [arXiv:1408.1810]

Sobrinho, J. L. G. & Augusto, P. 2020, *Stellar mass Primordial Black Holes as Cold Dark Matter*, MNRAS, 496, 60. doi:10.1093/mnras/staa1437

Sobrinho, J. L. G., Augusto, P., & Gonçalves, A. L. 2016, *New thresholds for primordial black hole formation during the QCD phase transition*, MNRAS, 463, 2348. doi:10.1093/mnras/stw2138

Sobrinho J. L. G., 2003, *Possibilidade de detecção directa de Buracos Negros por radiação electromagnética*, Tese submetida nas Provas de Aptidão Pedagógica e Capacidade Científica para habilitação à categoria de Assistente, Universidade da Madeira

Sobrinho, J. L. G. 2011, *The possibility of primordial black hole direct detection*, Ph.D. Thesis, Universidade da Madeira, `http://digituma.uma.pt/handle/10400.13/235`.

The LIGO Scientific Collaboration, the Virgo Collaboration, Abbott, R., et al. 2020, *GW190412: Observation of a Binary-Black-Hole Coalescence with Asymmetric Masses*, [arXiv:2004.08342]

Thompson, T. A., Kochanek, C. S., Stanek, K. Z., et al. 2019, *A noninteracting low-mass black hole-giant star binary system*, Science, 366, 637. doi:10.1126/science.aau4005